tin polyclonal antibody (Santa Cruz Biotechnology, Santa Cruz, CA), final dilution of 1:50, at 37°C for 30 minutes. The cells were then incubated with the secondary antibody (FITC-conjugated goat anti-rabbit IgG; H+L; Jackson ImmunoResearch Laboratory, West Grove, PA), with a final dilution of 1:50, at 37°C for 30 minutes and incubated with 10 μg/mL of propidium iodide at 37°C for 10 minutes to visualize the nucleus. The cells were observed under an Olympus Fluoview confocal laser-scanning microscope (Olympus, Tokyo, Japan).

RT-PCR Analysis

To study *Col7a1* mRNA expression in dental epithelial cells and ameloblasts, total RNA from tooth buds or cultured dental epithelial cells was extracted using the RNeasy Mini Kit (Qiagen, Tokyo, Japan) according to the manufacturer's instructions. RNA concentration was measured spectrophotometrically and samples were stored at −80°C until being used for reverse transcription-PCR (RT-PCR). We reverse transcribed RNA using SuperScript II (Invitrogen, Carlsbad, CA) according to the manufacturer's instructions. The following primers specific for mouse *Col7a1* sequence (NM: 007738) were used for RT-PCR: 5′-CGAGGAAGAGATGGTGAAGC-3′ (RT-F), and 5′-TTGCCTGAAGCACCATGTAG-3′ (RT-B). As a control, we used the primers for mouse glyceraldehyde-3-phosphate dehydrogenase (GAPDH; NM: 001001303): 5′-TTAGCCCCC CTGGCCAAGG-3′ (mGAPDH-F) and 5′-CTTACTCCTTGGAGGCCATG-3′ (mGAPDH-B), which amplified a 541-bp fragment.

Real-Time RT-PCR Analysis

To quantitatively analyze the mRNA expression levels of tooth formation–associated proteins [ie, amelogenin, ameloblastin, enamelin, tuftelin, enamelysin, and dentin sialophosphoprotein (DSPP)], in tooth buds from the *Col7a1*$^{+/+}$, *Col7a1*$^{-/-}$, and COL7-rescued mice, cDNA samples were analyzed using the ABI Prism 7000 Sequence Detection System (Applied Biosystems, Foster City, CA). Primers and probes specific for amelogenin, ameloblastin, enamelin, tuftelin, enamelysin, DSPP, and the control housekeeping genes coding glyceraldehyde-3-phosphate dehydrogenase (GAPDH) and β-actin were obtained from the TaqMan Gene Expression Assay (Applied Biosystems; Probe ID: Mm00711644_g1, Mm00477485_m1, Mm00516922_m1, Mm00449139_m1, Mm00600244_m1, Mm00515666_m1, Mm99999915_gl, and Mm00607939_sl).

Differences between the mean cycle threshold (Ct) values of mRNA expression of tooth formation–associated proteins and those of GAPDH or ß-actin were calculated as $\Delta Ct_{Col7a1-/-\ mice} = Ct_{tooth\ protein} - Ct_{GAPDH\ (or\ other\ housekeeping\ genes)}$ and those of ΔCt for the *Col7a1*$^{+/+}$ teeth as $\Delta Ct_{calibrator} = Ct_{tooth\ protein} - Ct_{GAPDH\ (or\ other\ housekeeping\ genes)}$. We were able to obtain similar results from the GAPDH and β-actin standard; thus, we describe the results of the GAPDH standard in the present study. Final results for *Col7a1*$^{-/-}$ tooth samples/*Col7a1*$^{+/+}$ tooth samples (%) were determined by $2^{-(\Delta^{Ct\ Col7a1-/-} - \Delta^{Ctcalibrator})}$.

Using similar methods, we quantitatively analyzed the tooth formation–associated protein mRNA expression levels in the primary dental epithelial cells cultured from the *Col7a1*$^{+/+}$, *Col7a1*$^{-/-}$, and COL7-rescued mice.

Western Blot Analysis

To study COL7 and laminin332 expression in the ameloblasts cultured from the *Col7a1*$^{+/+}$ and *Col7a1*$^{-/-}$ mice, we used proteins extracted from cultured ameloblasts prepared with radioimmunoprecipitation assay buffer comprising 50 mmol/L Tris-HCl (pH 7.5), 150 mmol/L NaCl, 1% Nonidet P-40, 0.5% deoxycholate, 0.1% SDS, and Roche Protease Cocktail Tablet (Roche, Basel, Switzerland). The proteins were fractionated by SDS-PAGE and transferred to polyvinylidene difluoride membranes for immunoblotting. Membrane blocking and incubation with antibodies were performed in Tris-buffered saline with 2% nonfat dry milk. The following primary antibodies were used: anti-mouse COL7 polyclonal antibody (Calbiochem; final dilution of 1:1000), anti-mouse laminin332 polyclonal antibody (Abcam; final dilution of 1:1000), and anti-mouse β-actin monoclonal antibody (Sigma, St. Louis, MO; final dilution of 1:1000). The following secondary antibodies were used: horseradish peroxidase–conjugated goat anti-rabbit IgG or horseradish peroxidase–conjugated goat anti-mouse IgG (Invitrogen; final dilution of 1:5000). Signals were revealed with chemiluminescence reagents and photographed by LAS-1000 mini digital camera (Fujifilm, Tokyo, Japan).

Results

Structural Defects of the Enamel in the RDEB Patient

We examined teeth from a 9-year-old female patient with RDEB resulting from COL7 deficiency (Figure 1, I–P). Under macroscopic observation, dental caries with a whitish appearance was widely seen on the enamel surface of permanent premolars (Figure 1, I and J). The enamel surface of the patient was rough and pitted under SEM (Figure 1, K and L). In the labiolingual section of the patient's teeth, the overall structure of the enamel layer was similar to healthy control at the light microscopic level (Figure 1, M and N). However, ultrastructurally, the pattern of enamel rods was disrupted in the enamel layer in contrast with the normal human control (Figure 1, O and P).

COL7 Expression Pattern in the EMJ of Teeth in the Col7a1$^{-/-}$ *Mice*

To clarify COL7 expression during tooth formation, we immunostained tissue sections of neonatal incisors and molars. In the incisors, we were able to observe the presecretory and secretory stages of tooth formation (Figure 2D). COL7 was expressed in the EMJ between ameloblasts and odontoblasts at the presecretory stage in

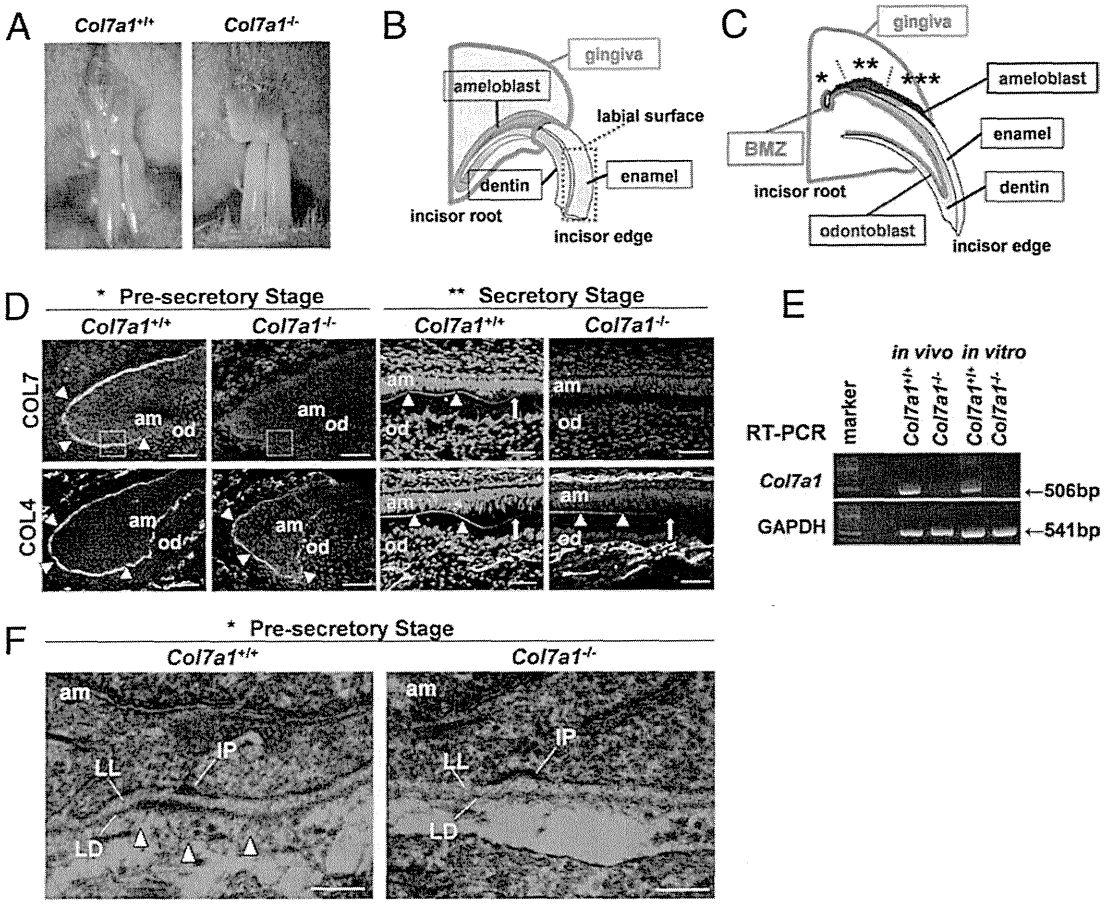

Figure 2. COL7 expression in the tooth of *Col7a1*$^{+/+}$ mice, and COL7 absence in the tooth of *Col7a1*$^{-/-}$ mice. **A:** Mice incisors are continuously elongating; shown are the teeth of 4-month-old mice. **B** and **C:** Schematic of mouse upper incisor. A sagittal section is shown in C. In the root of these incisors, teeth develop through three main stages: i) presecretory (*); ii) secretory (**); and iii) maturation (***). In the presecretory stage, epithelial cells differentiate into ameloblasts (blue), and mesenchymal cells differentiate into odontoblasts (green). In the secretory stage, ameloblasts and odontoblasts secrete enamel matrix (sky blue) and dentin (gray). In the maturation stage, mineralization of the enamel matrix to enamel (yellow) occurs. Red line: basement membrane zone (BMZ). **D:** Immunofluorescence staining for COL7 in neonatal mice incisors reveals that COL7 is expressed in the EMJ between ameloblasts and odontoblasts at the presecretory stage (**white arrowheads**) of a *Col7a1*$^{+/+}$ mouse. At the secretory stage, COL7 expression (**white arrowheads**) is gradually reduced and becomes absent (**white arrow**). In the *Col7a1*$^{-/-}$ mice, no COL7 staining is observed in any part of the EMJ. COL4 is expressed in the EMJ (**white arrowheads**) in both *Col7a1*$^{+/+}$ and *Col7a1*$^{-/-}$ mice incisors. At the secretory stage of incisors, the basement membrane becomes discontinuous, and COL4 expression is gradually reduced and absent in places (**white arrow**). Scale bars = 40 μm. Shown are neonatal mice incisors. **E:** RT-PCR assay reveals that *Col7a1* mRNA (506-bp band) is expressed in *Col7a1*$^{+/+}$ mouse teeth (**left lane**) and cultured ameloblasts from *Col7a1*$^{+/+}$ mice (**second right lane**). *Col7a1* mRNA is not expressed in either *Col7a1*$^{-/-}$ mouse teeth (**second left lane**) or in cultured ameloblasts from *Col7a1*$^{-/-}$ mice (**right hand lane**). Shown are 3-day-old mice incisors and molars. **F:** Ultrastructural features of the basement membrane zone at the presecretory stage. Anchoring fibrils, which anchor lamina densa to the underlying mesenchymal tissue, and anchoring filaments crossing the lamina lucida are seen in the *Col7a1*$^{+/+}$ mouse (**left, white arrowheads**), but there are no apparent anchoring fibrils in the *Col7a1*$^{-/-}$ mice, even though the lamina densa is normally formed (**right**). am, ameloblasts; IP, inner attachment plaques; LD, lamina densa; LL, lamina lucida; od, odontoblast. Scale bar = 250 nm. Shown are neonatal mice molars.

wild-type (*Col7a1*$^{+/+}$) mice and heterozygous (*Col7a1*$^{+/-}$) mice (data not shown). Due to elongation of Tomes' processes, the basement membrane became discontinuous, and COL7 expression was gradually reduced and became absent in places at the secretory stage. In molars, we were able to observe the presecretory stage of tooth formation. In the molars of *Col7a1*$^{+/+}$ and *Col7a1*$^{+/-}$ mice, COL7 was expressed in the EMJ between ameloblasts and odontoblasts at the presecretory stage (data not shown).

In the *Col7a1*$^{-/-}$ mice, COL7 expression was not observed in the EMJ underlying the ameloblasts at any stage of tooth development.

We also studied COL4 expression during tooth formation (Figure 2D) because COL4 is a major protein component of the lamina densa in the EMJ.[3] In the *Col7a1*$^{+/+}$, *Col7a1*$^{+/-}$, and *Col7a1*$^{-/-}$ mice, COL4 was expressed in the EMJ between ameloblasts and odontoblasts at the presecretory stage. At the secretory stage, the basement membrane became discontinuous, and COL4 expression was gradually reduced and absent in places.

In addition, we examined expression of laminin332, a component of anchoring filaments, during tooth formation, because this protein interacts directly with COL7 and is already known to affect ameloblast differentiation. In the *Col7a1*$^{+/+}$, *Col7a1*$^{+/-}$, and *Col7a1*$^{-/-}$ mice, laminin332 was seen at the EMJ between ameloblasts and odontoblasts at the presecretory stage (data not shown). At the secretory stage, laminin332 staining was weak and negative in places (data not shown).

We subsequently analyzed mouse *Col7a1* mRNA expression in tooth buds or cultured dental epithelial cells by RT-PCR (Figure 2E). The 506-bp fragment of mouse *Col7a1* mRNA was detected in the *Col7a1*$^{+/+}$ mouse

teeth *in vivo* and in cells cultured from the *Col7a1*$^{+/+}$ mouse teeth *in vitro*, but mouse *Col7a1* mRNA was not detected in either teeth or cultured cells from the *Col7a1*$^{-/-}$ mice (Figure 2E).

In addition, we analyzed mouse COL7 and laminin332 protein expression in cultured dental epithelial cells by Western blotting. COL7 was not detected in cell lysates from the *Col7a1*$^{+/+}$ or *Col7a1*$^{-/-}$ mice (data not shown), although weak laminin332 protein expression was detected in the cultured cells from the *Col7a1*$^{+/+}$ and *Col7a1*$^{-/-}$ mice (data not shown).

The basement membrane on the basal surface of the ameloblasts separates the ameloblasts from mesenchymal tissue/odontoblasts. Beneath the lamina densa, most of the COL7 molecules form semicircular loop structures called anchoring fibrils whose terminals originate and terminate in the lamina densa, similar to those at the dermoepidermal junction of the skin.[22]

Ultrastructurally, in the underlying mesenchymal tissue, anchoring fibrils enable the lamina densa to link or encircle mesenchymal collagen fibers or other components to anchor the basal lamina to underlying structures. Thin anchoring filaments cross the lamina lucida zone, subjacent to hemidesmosomes, and extend into the lamina densa in the *Col7a1*$^{+/+}$ mice (Figure 2F, left) and the *Col7a1*$^{+/-}$ mice (data not shown). In the *Col7a1*$^{-/-}$ mice, there were no apparent anchoring fibrils, even though the lamina densa was normally formed (Figure 2F, right).

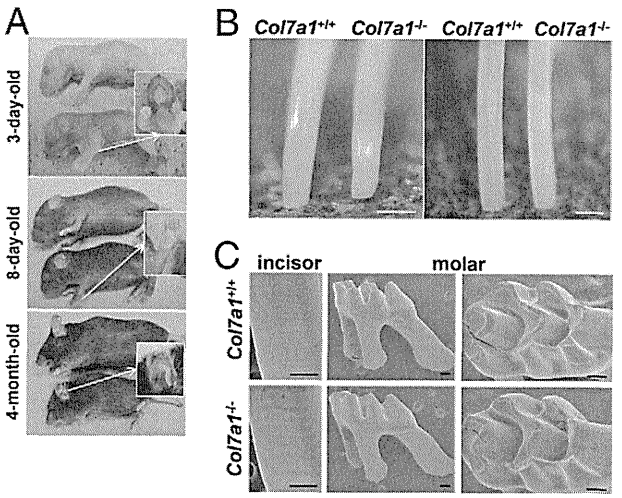

Figure 3. Dental phenotype of *Col7a1*$^{-/-}$ mice. **A:** Clinical presentation of *Col7a1*$^{-/-}$ mice (**lower**) compared with *Col7a1*$^{+/+}$ littermate (**upper**). Typical blister and scar seen on paws (**inset**). Malformed ears (**inset**). **B:** At 2 weeks of age, *Col7a1*$^{+/+}$ and *Col7a1*$^{-/-}$ mice have whitish incisors (**left**). There is no apparent difference in enamel shape and surface structure between these mice. At 4 months of age, incisors of the *Col7a1*$^{+/+}$ and the *Col7a1*$^{-/-}$ mice show similar yellowish color (**right**). There is also no apparent difference in shape and surface structure between incisors of the *Col7a1*$^{+/+}$ and *Col7a1*$^{-/-}$ mice. Scale bars: 500 μm. **C:** By SEM, the enamel surface of incisal teeth and molars in the *Col7a1*$^{+/+}$ and *Col7a1*$^{-/-}$ mice appear smooth and unpitted. In the molars, tooth wear is equal between *Col7a1*$^{+/+}$ and *Col7a1*$^{-/-}$ mice. Scale bars = 200 μm. Shown are 4-month-old mice incisors and molars.

Dental Phenotype of the Col7a1$^{-/-}$ *Mice*

The *Col7a1*$^{-/-}$ mice demonstrated a striking skin phenotype noted at birth or shortly thereafter: A large blister developed primarily on the ventral side of the mice, often extending to cover the extremities (Figure 3A). Some of the affected mice died within the first week of life from complications of the disease, whereas the others survived beyond the first week of life and demonstrated normal hair growth that appeared to coincide with lessening of the blistering tendency in the skin (Figure 3A).

At 2 weeks of age, shortly after eruption of incisors, the wild-type (*Col7a1*$^{+/+}$), heterozygous (*Col7a1*$^{+/-}$), and *Col7a1*$^{-/-}$ mice had whitish incisors (Figure 3B). There was no apparent difference in enamel shape and surface structure among these three types of mice under macroscopic observation. The COL7-rescued mice (mouse *Col7a1*$^{-/-}$, human *COL7A1*$^{+}$) had similar incisors, as did these three types of mice (data not shown). At 4 months of age, incisors of the *Col7a1*$^{+/+}$ and *Col7a1*$^{-/-}$ mice showed similar yellowish color. There was also no apparent difference in shape or surface structure between incisors of the *Col7a1*$^{+/+}$ and *Col7a1*$^{-/-}$ mice (Figure 3B). As for the oral mucosa and soft tissue manifestations, the *Col7a1*$^{-/-}$ mice showed extreme fragility of the oral and perioral mucosa. In the maxillary mucosa, the continual process of blister formation and healing resulted in loss of normal anatomical oral features, such as the palatal rugae, leaving a smooth and ulcerated roof of the mouth (data not shown).

Under SEM, the enamel surfaces of incisal teeth and molars in the *Col7a1*$^{+/+}$(Figure 3C), *Col7a1*$^{+/-}$ (data not shown), and *Col7a1*$^{-/-}$ (Figure 3C) mice all appeared smooth and unpitted. In the molars, tooth wear was equal between the *Col7a1*$^{+/+}$ and *Col7a1*$^{-/-}$ mice. In transverse sections of the *Col7a1*$^{-/-}$ mice incisors (Figure 4, C and F), the enamel rod inclination was irregular, and the rods had lost the normal network arrangement that was seen in the *Col7a1*$^{+/+}$ mice (Figure 4, B and E) and *Col7a1*$^{+/-}$ mice (data not shown). In the COL7-rescued mice (*Col7a1*$^{-/-}$, human *COL7A1*$^{+}$ mice), enamel rod formation was restored to normal (Figure 4, D and G), confirming that the enamel changes were caused by COL7 deficiency.

Chemical and Mineralization Analysis of the Teeth

Backscatter electron images of the transverse labiolingual sections of the incisors in the *Col7a1*$^{+/+}$, *Col7a1*$^{+/-}$, and *Col7a1*$^{-/-}$ mice revealed calcium and phosphorus to be homogeneously distributed in all samples (data not shown). Iron was also homogeneously distributed on the enamel surface. There were no significant differences in the atomic concentrations of calcium and phosphorus between enamel of 4-month-old *Col7a1*$^{+/+}$ and *Col7a1*$^{-/-}$ mice. The calcium concentration was 25.4 ± 1.2% for *Col7a1*$^{+/+}$ and 24.9 ± 1.5% for *Col7a1*$^{-/-}$, and the phosphorus concentration was 19.6 ± 0.60% for *Col7a1*$^{+/+}$ and 18.9 ± 1.6% for *Col7a1*$^{-/-}$. Energy-dispersive X-ray spectrometry spectra at a number of spots showed that there was no significant difference between the *Col7a1*$^{+/+}$ and *Col7a1*$^{-/-}$ mice in terms of the concentrations of calcium,

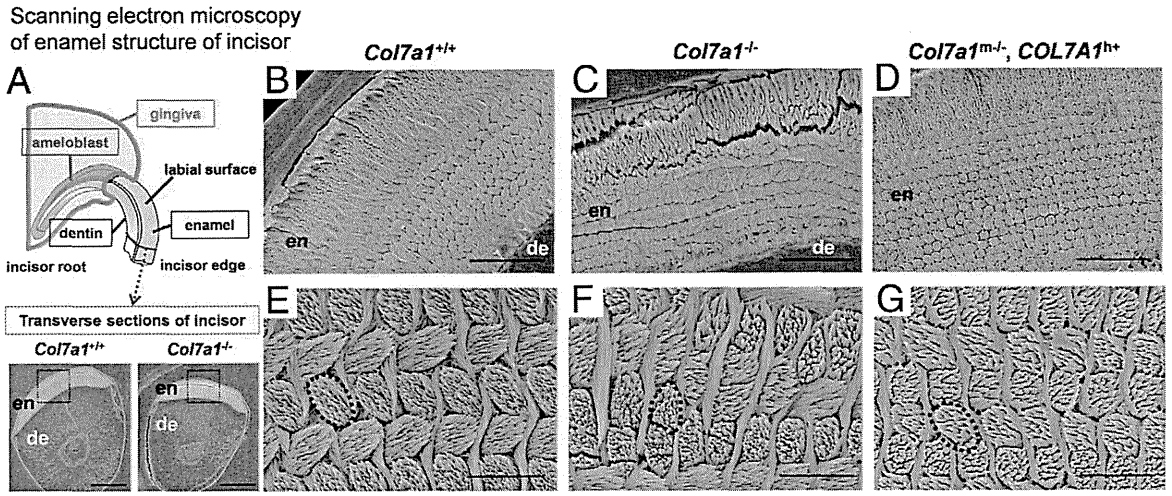

Figure 4. SEM of the transverse sections of incisors. **A:** Model of an upper incisor. A transverse section of the incisor (green line) is shown at the **bottom**. The enamel layer, indicated by the rectangle, is enlarged in **B** and **C**. High-power views of the enamel rod inclinations in **B–D** are shown in **E–G**, respectively. **B–G:** In the *Col7a1*$^{-/-}$ mouse, irregular inclinations of enamel rods without a normal network arrangement are observed (**C** and **F**), in contrast to the regular network of enamel rods observed in the *Col7a1*$^{+/+}$ incisor (**B** and **E**). The normal, regular network of enamel rods has been restored in the COL7-humanized mouse (**D** and **G**). **Black dotted line** in **E–G:** enamel rod. de, dentin; en, enamel. Scale bars: 100 μm (**A**); 20 μm (**B–D**); 5 μm (**E–G**). Shown are 15-day-old mice incisors.

phosphorus, iron, and other ions on the surface of the enamel (data not shown).

To compare the mineralization patterns of teeth between the *Col7a1*$^{+/+}$, *Col7a1*$^{+/-}$, and *Col7a1*$^{-/-}$ mice, micro-CT scanning was performed on the maxillomandibular incisors. Calcifications of skull and incisor were clearly visible. In the incisors of the *Col7a1*$^{+/+}$, *Col7a1*$^{+/-}$, and *Col7a1*$^{-/-}$ mice, the radio-opacity of the enamel increased gradually toward the incisal edge, from the enamel secretory stage to the maturation stage. Mineralization reached its maximum at the incisal edge (data not shown). To objectively evaluate the mineralization level in the enamel layers, we measured the mean CT number of the incisal edge in Hounsfield units (HU). There was no significant difference in the CT number of the incisal edge between the 20-day-old *Col7a1*$^{+/+}$ and *Col7a1*$^{-/-}$ mice. That number was 1070.26 ± 33.40 HU for *Col7a1*$^{+/+}$ and 1078.61 ± 33.51 HU for *Col7a1*$^{-/-}$. These results show that mineralization of the enamel in the *Col7a1*$^{-/-}$ incisors was similar to that in the *Col7a1*$^{+/+}$ incisors.

Defective Amelogenesis in Col7a1$^{-/-}$ *Mice*

We observed the tooth development at each of the three stages of enamel formation: presecretory, secretory, and maturation (Figure 5, A–C). There is no apparent blistering in the EMJ between ameloblasts and odontoblasts in the *Col7a1*$^{+/+}$, *Col7a1*$^{+/-}$, and *Col7a1*$^{-/-}$ mice. Ameloblast size and enamel matrix thickness in the *Col7a1*$^{-/-}$ mice were similar to those in the *Col7a1*$^{+/+}$ and *Col7a1*$^{+/-}$ mice (Figure 5, D, F, H, and J). The Tomes' processes of the *Col7a1*$^{+/+}$ and *Col7a1*$^{+/-}$ mice were triangular and orderly. By contrast, the processes of the *Col7a1*$^{-/-}$ mice were deformed and difficult to clearly visualize in H&E-stained sections (Figure 5, D and F).

Furthermore, enamel formation of the teeth of the *Col7a1*$^{+/+}$, *Col7a1*$^{+/-}$, and *Col7a1*$^{-/-}$ mice was studied ultrastructurally. In the presecretory to the early secretory stage, the overall structure of ameloblasts was similar between the *Col7a1*$^{+/+}$ and *Col7a1*$^{-/-}$ mice. In the presecretory stage, anchoring fibrils were identified in the *Col7a1*$^{+/+}$ mice (Figure 2F, left) and *Col7a1*$^{+/-}$ mice, but not in the *Col7a1*$^{-/-}$ mice (Figure 2F, right). However, in the early secretory stage, only thin filamentous material was observed beneath the basal lamina at the EMJ in the *Col7a1*$^{+/+}$, *Col7a1*$^{+/-}$, and *Col7a1*$^{-/-}$ mice (data not shown). In the secretory stage, secretory ameloblasts appeared as tall columnar cells with intact Tomes' processes producing enamel matrix in the *Col7a1*$^{+/+}$ (Figure 5E) and *Col7a1*$^{+/-}$ (data not shown) mice.

In the *Col7a1*$^{-/-}$ mice, the Tomes' processes were disorganized and irregular in size and width, showing a less prominent appearance compared with those of the *Col7a1*$^{+/+}$ mice (Figure 5G). There was no obvious abnormality in the other structural components of the ameloblasts. During the secretory stage, the electron density of the enamel matrix of the *Col7a1*$^{-/-}$ mice was similar to that of *Col7a1*$^{+/+}$ and *Col7a1*$^{+/-}$ mice.

In the maturation stage, mature ameloblasts were columnar cells that had rough endoplasmic reticulum, lysosomes, mitochondria, small vacuoles and Golgi apparatuses in the apical and mid portions. The cell structure and organelles of *Col7a1*$^{-/-}$ mature ameloblasts appeared normal, but the enamel rods were rougher and more irregularly distributed (Figure 5, J and K) than those of the *Col7a1*$^{+/+}$ mice (Figure 5, H and I) and *Col7a1*$^{+/-}$ mice (data not shown).

In the COL7-rescued mice (*Col7a1*$^{-/-}$, human *COL7A1*$^{+}$ mice), the overall structure of ameloblasts was similar to those in the *Col7a1*$^{+/+}$ mice, and the Tomes' processes were restored to normal (data not shown).

We performed Berlin blue staining in the maturation stage of 11-day-old *Col7a1*$^{+/+}$ and *Col7a1*$^{-/-}$ mice teeth. In both mice, positive staining of Berlin blue was detected in the ameloblast cytosol, indicating the accumulation of

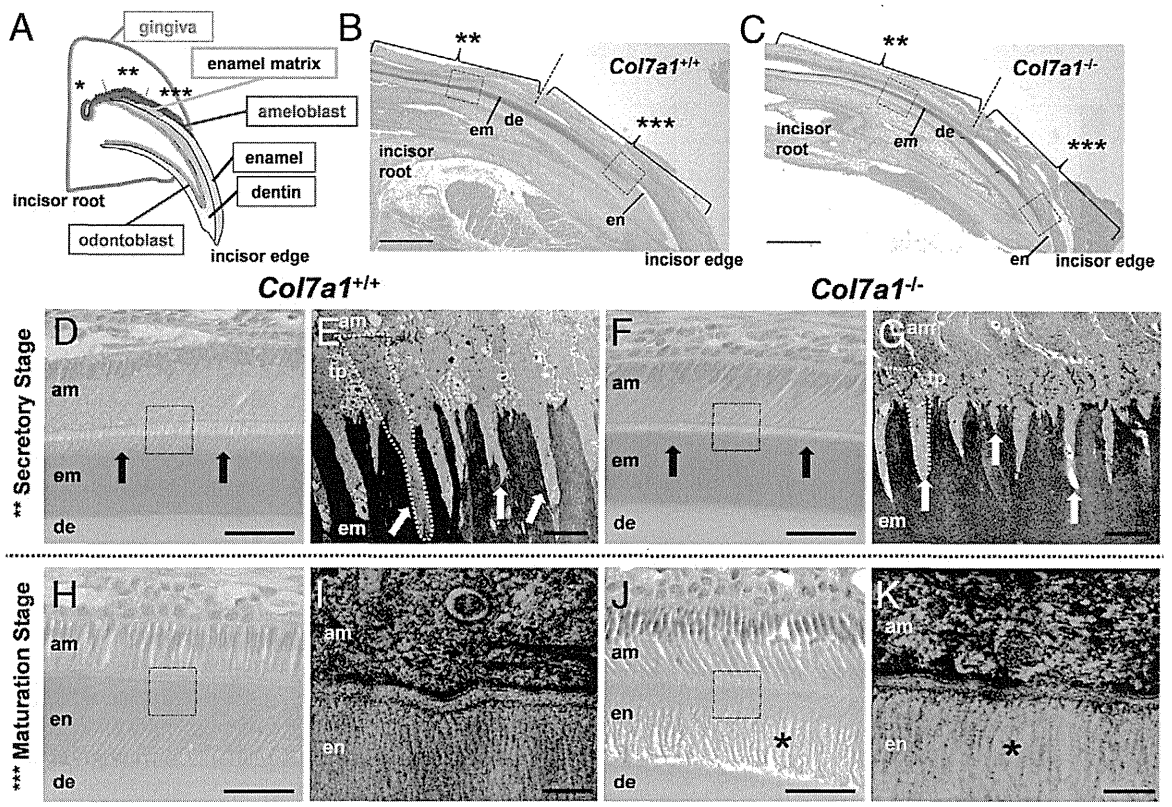

Figure 5. Malformed Tomes' processes in *Col7a1*$^{-/-}$ mice and defective amelogenesis in *Col7a1*$^{-/-}$ mice. **A:** Three stages of ameloblast differentiation are observed in sagittal sections of mice incisors: i) presecretory stage (**asterisk**); ii) secretory stage (**double asterisk**); and iii) maturation stage (**triple asterisk**). **B** and **C:** The secretory and maturation stage of enamel formation is enlarged in **D–K**. **Rectangles with red** and **blue dotted lines** are enlarged in **D–G** and in **H–K**, respectively. **D–G:** At the secretory stage, Tomes' processes have formed and enamel matrix is produced by ameloblasts. **D** and **F:** In the secretory stage, the processes of ameloblasts are malformed and blurred (**arrows**) in the *Col7a1*$^{-/-}$ mouse (**F**), compared with well-organized lattice-like structures of the Tomes' processes (**arrows**) in the *Col7a1*$^{+/+}$ mice (**D**). The thickness of the enamel matrix seems similar between the *Col7a1*$^{+/+}$ (**D**) and *Col7a1*$^{-/-}$ (**F**) mice. **E** and **G:** At the secretory stage, in the *Col7a1*$^{-/-}$ mice, the Tomes' processes (**white arrows**) are hypoplastic and irregular in size and width, showing a less prominent appearance compared with normal Tomes' processes in the *Col7a1*$^{+/+}$ mouse. **H–K:** At the maturation stage, the cell structure and organelles of *Col7a1*$^{-/-}$ mature ameloblasts appear normal; however, the enamel rods are rough and irregularly distributed (**asterisk**) compared with those of the *Col7a1*$^{+/+}$ mice. am, ameloblast; de, dentin; em, enamel matrix; en, enamel; od, odontoblast; tp, Tomes' processes. Scale bars: 400 μm (**B** and **C**); 40 μm (**D**, **F**, **H**, and **J**); 4 μm (**E** and **G**); 200 nm (**I** and **K**). Shown are 5-day-old mice incisors.

iron, during the maturation stage (data not shown). There was no obvious difference in the Berlin blue staining patterns between the *Col7a1*$^{+/+}$ and *Col7a1*$^{-/-}$ mice, suggesting that the aberrant differentiation of ameloblasts in the *Col7a1*$^{-/-}$ mice did not affect iron metabolism.

Assay of Ameloblast Differentiation

We examined the expression of enamel proteins in the teeth *in vivo* and in cultured dental epithelial cells *in vitro* using real-time RT-PCR analysis.[23–25] mRNA expression of the major enamel proteins produced by ameloblasts *in vivo*, including amelogenin, ameloblastin, enamelin, enamelysin, and DSPP, was significantly decreased in the *Col7a1*$^{-/-}$ teeth, except for the expression of tuftelin (Figure 6A), which was only slightly reduced. Real-time RT-PCR analysis demonstrated that in the teeth of COL7-rescued mice, *in vivo* mRNA expression of the major enamel proteins was restored (data not shown). In dental epithelial cells cultured from the *Col7a1*$^{+/+}$ mice, mRNA expression of amelogenin, ameloblastin, and tuftelin was confirmed, although mRNA expression of enamelin, enamelysin, and DSPP was absent. In the *Col7a1*$^{-/-}$ mice, mRNA expression of amelogenin and tuftelin in cultured cells were significantly lower than in the *Col7a1*$^{+/+}$ mice. Ameloblastin expression in the cultured *Col7a1*$^{-/-}$ cells was higher than in the cells cultured from the *Col7a1*$^{+/+}$ mice (data not shown). Real-time RT-PCR analysis revealed that, in the COL7-rescued mice, mRNA expression of amelogenin and tuftelin in cultured cells was restored (data not shown). Immunocytological examinations revealed granular expression of amelogenin in the ameloblasts cultured from the *Col7a1*$^{+/+}$ (Figure 6B) and COL7-rescued mice (data not shown), although no expression of amelogenin was observed in the cells cultured from the *Col7a1*$^{-/-}$ mice (Figure 6C). Expression of ameloblastin was similar in cells cultured from the *Col7a1*$^{+/+}$, *Col7a1*$^{-/-}$, and COL7-rescued mice (data not shown).

Discussion

RDEB is a hereditary blistering skin disease with tissue separation occurring beneath the lamina densa of the epidermal basement membrane zone. RDEB is characterized by mucocutaneous blistering in response to minor

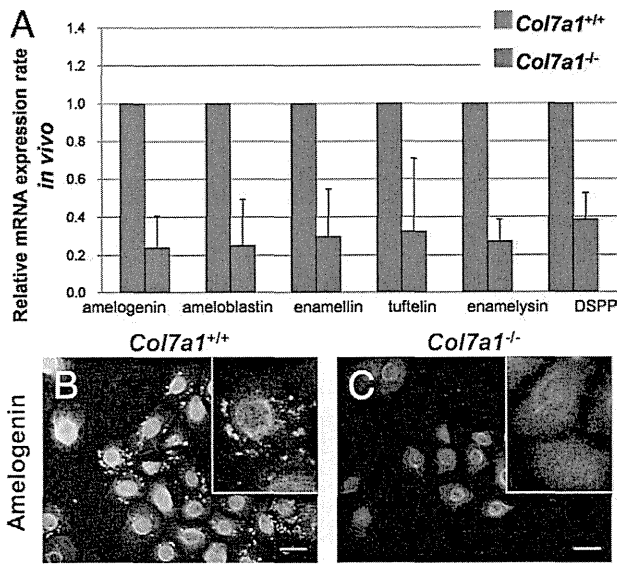

Figure 6. Expression of enamel proteins in *Col7a1*$^{-/-}$ ameloblasts. **A:** mRNA expression of all of the enamel proteins examined (amelogenin, ameloblastin, enamelin, tuftelin, enamelysin, and DSPP) was down-regulated in ameloblasts of the teeth of the *Col7a1*$^{-/-}$mice *in vivo.* (3-, 4-, and 5-day-old *Col7a1*$^{+/+}$ mice incisors and molars, $n = 3$; 3-, 4-, and 5-day-old *Col7a1*$^{-/-}$ mice incisors and molars, $n = 3$). **B** and **C:** Protein expression (FITC, green) of amelogenin is decreased in ameloblasts cultured from the *Col7a1*$^{-/-}$ mice (**C**), relative to that in ameloblasts cultured from the *Col7a1*$^{+/+}$ mice (**B**). **Insets:** high-power views. Scale bars = 10 μm. Shown are 8-day-old mice incisors.

trauma, followed by ulceration and scarring mainly in the hands and feet, joint contractures, strictures of the esophagus and dental abnormalities.[11] Molecular genetic studies have revealed that RDEB is caused by mutations in the gene that encodes COL7, a major component of anchoring fibrils.[11,26,27] Most RDEB patients exhibit oral mucous membrane blistering, and prevalent tooth abnormalities with caries.[12,13]

The present study revealed that the secretory ameloblasts of the *Col7a1*$^{-/-}$ mice lacked normal enamel protein-secreting Tomes' processes and exhibited disturbed enamel matrix secretion, which resulted in imperfect amelogenesis demonstrated by malformed enamel rods and irregular enamel matrix (Figure 7).

Mice have only one set of dentition, whereas humans have two: primary and secondary. As for the total number and the type of teeth, mice have 16 teeth, and these are classified as incisors and molars, whereas humans usually have 20 primary teeth and 32 permanent teeth, and these are classified as incisors, canines, premolars and molars. Due to these differences, the tooth abnormalities demonstrated in *Col7a1*$^{-/-}$ mice are not perfectly analogous to the tooth abnormality in human RDEB patients, because RDEB affects all types of teeth and both the primary and secondary dentition in humans. However, the physiological processes of enamel formation are similar in all types of teeth of both human and mouse.[28,29] Thus, we believe that the present *Col7a1*$^{-/-}$ mice are a practical and useful model for studying RDEB dental abnormalities.

Some of the *Col7a1*$^{-/-}$ mice showed growth retardation as early as 3 days of age and died within the first week of life from complications of the disease. A sequence of events associated with the development of the teeth begins with neural crest cell migration at embryonic days 8.5 to 10 (E8.5 to E10); formation of the dental lamina is at E12.[30] Ameloblast differentiation and crown formation are observed in newborn postnatal mice. Thus, we believe that the present *Col7a1*$^{-/-}$ mouse is an adequate model for studying the pathomechanisms of enamel defects caused by COL7 deficiency.

Micro-CT observation demonstrated that enamel calcification patterns were similar between the *Col7a1*$^{-/-}$ and *Col7a1*$^{+/+}$ mice. In addition, similar deposition patterns of chemical components were revealed in the enamel of the *Col7a1*$^{-/-}$ and *Col7a1*$^{+/+}$ mice by SEM–energy-dispersive X-ray spectrometry. With Berlin blue staining, iron accumulation patterns were also identical in

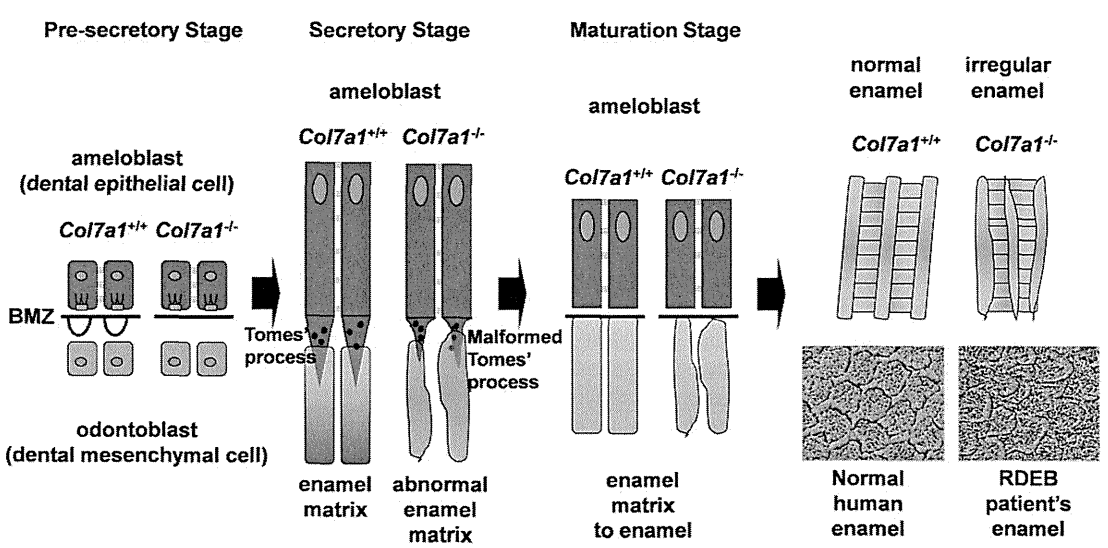

Figure 7. Diagrams of normal enamel formation in *Col7a1*$^{+/+}$ mice and defective enamel formation in *Col7a1*$^{-/-}$ mice. At the presecretory stage, hypoplasia of anchoring fibrils is the only apparent abnormality in the *Col7a1*$^{-/-}$ teeth (**right**), whereas anchoring fibrils are seen in the *Col7a1*$^{+/+}$ teeth (**left**). From the secretory to the maturation stages, normal enamel matrix is formed by Tomes' processes, resulting in intact enamel formation in the *Col7a1*$^{+/+}$ teeth (**left**). In the *Col7a1*$^{-/-}$ teeth (**right**), disrupted Tomes' processes produce disturbed enamel matrix, leading to irregular enamel formation.

the ameloblasts of *Col7a1*$^{-/-}$ and *Col7a1*$^{+/+}$ incisors. Deposition of iron and other ions is known to occur with maturation of the enamel matrix and mineralization at maturation stage, and the present results suggest that disturbed differentiation of ameloblasts in *Col7a1*$^{-/-}$ mice does not affect the mineralization in tooth enamel formation.

Subsequently, we studied the developmental processes of the teeth in the *Col7a1*$^{-/-}$ mice. The teeth develop through the presecretory, secretory, and maturation stages.[31] At the presecretory stage, hypoplasia of anchoring fibrils was the only apparent abnormality in the *Col7a1*$^{-/-}$ mice teeth. The Tomes' processes are known to be involved in the secretion of enamel matrix,[31] and, in ameloblasts in the secretory stage, disturbed Tomes' process formation was observed in the *Col7a1*$^{-/-}$ mice, although enamel matrix was seen around the malformed Tomes' processes.

Ameloblasts at the maturation stage showed no apparent abnormalities, although the crystal structure of the enamel matrix was disturbed in the *Col7a1*$^{-/-}$ mice. SEM revealed that enamel rods were malformed and irregular in the enamel of the *Col7a1*$^{-/-}$ mice. These morphological abnormalities were not observed in the rescued COL7-humanized mice, thus suggesting that the abnormalities were direct effects of the COL7 deficiency. These results clearly indicate that tooth malformation in *Col7a1*$^{-/-}$ mice, and probably in *COL7A1*-deficient RDEB patients, is caused by aberrant differentiation of ameloblasts. These abnormal ameloblasts lacked normal Tomes' processes and secreted reduced amounts of enamel matrix, resulting in irregular enamel rod inclination (Figure 7).

The enamel rod inclination of teeth from the RDEB patient was irregular in the enamel layer, compared with that of a normal human control, although she does not show a complete absence of COL7. These abnormalities are most likely a consequence of a lack of COL7 causing aberrant ameloblast differentiation, similar to those in *Col7a1*$^{-/-}$ mice. Ameloblasts in *Col7a1*$^{-/-}$ mice express reduced amounts of amelogenin, ameloblastin, and other enamel proteins. These enamel proteins are secreted from Tomes' processes at the secretory stage and form the enamel matrix. Thus, the results of the present *in vivo* enamel protein expression study further support the idea that ameloblast differentiation, especially the formation of enamel protein-secreting Tomes' process, is disturbed in *Col7a1*$^{-/-}$ mice. Amelogenin is the most abundant of the proteins secreted by the ameloblasts, accounting for approximately 90% of total enamel protein. Mice null for amelogenin have been reported to produce hypoplastic enamel matrix without well-defined enamel rods.[32]

Ameloblasts cultured without interaction with mesenchymal tissue cannot differentiate sufficiently to form columnar epithelium.[33] In the present study, such insufficiently differentiated ameloblasts expressed mRNA for amelogenin, ameloblastin, and tuftelin, but not other enamel proteins, including enamelin and enamelysin. Cultured ameloblasts from *Col7a1*$^{-/-}$ mice expressed ameloblastin mRNA almost as much as ameloblasts from *Col7a1*$^{+/+}$ mice do, although *Col7a1*$^{-/-}$ cells expressed reduced amounts of amelogenin and tuftelin mRNA. We confirmed by RT-PCR analysis that *Col7a1* mRNA is expressed from cultured ameloblasts (Figure 2E), although we were unable to detect COL7 protein expression from cultured ameloblasts by Western blotting. We consider that the expressed amount of COL7 protein was so tiny that we could not detect a COL7 band by Western blotting in the present study. COL7 expression might be associated with ameloblast differentiation, and COL7 deficiency in *Col7a1*$^{-/-}$ cells might lead to the decreased expression of the major ameloblast differentiation-associated proteins, although there is no direct evidence of regulatory effects by COL7 in the differentiation of cultured ameloblasts.

In the *Col7a1*$^{-/-}$ mice, ameloblast differentiation was retarded, resulting in malformation of Tomes' processes. The present results in *Col7a1*$^{-/-}$ mice clearly demonstrate that COL7, a component of the anchoring fibrils involved in basement membrane adhesion, also regulates differentiation of odontogenic epithelial cells including ameloblasts and plays essential role in enamelization.

COL17 is known to be important components of hemidesmosomes. COL17 deficiency results in junctional EB, a hereditary blistering skin disease with tissue separation occurring within the lamina lucida of the epidermal basement membrane zone. Remarkable abnormalities, including disturbance of ameloblast differentiation and reduced enamel deposition, have also been reported in the incisors of COL17-disrupted mice.[4] These facts further support the idea that interactions between ameloblasts and mesenchymal tissue via the basement membrane are crucial for ameloblast differentiation and function. Ultrastructural changes of Tomes' processes have been observed in COL17-disrupted *Col17a1*$^{-/-}$ mice,[4] similar to those observed in *Col7a1*$^{-/-}$ mice in the present study. During the maturation stage, teeth calcification was delayed in the *Col17a1*$^{-/-}$ mice, and reduced iron deposition was revealed in the enamel of *Col17a1*$^{-/-}$ incisors,[4] but not of *Col7a1*$^{-/-}$ mice in our study. These findings suggest that a lack of COL7 and a lack of COL17 have similar detrimental effects on ameloblast differentiation and enamel formation, although COL17 deficiency appears to have more severe disruptive effects on enamel epithelium than COL7 deficiency has.

Concerning laminin332, another causative molecule of junctional EB, patients with laminin332 deficiency also show abnormal tooth formation (amelogenesis imperfecta).[6] Laminin332-deficient mice exhibit disturbed ameloblast differentiation and reduced enamel deposition.[5] During the maturation stage of teeth, tissue organization was completely disrupted in the enamel epithelium of the laminin332-deficient mice. Thus, laminin332 is thought to play an important role in regulating ameloblast differentiation during tooth development.[5] In addition, it is known that COL7 interacts with laminin332 at the EMJ.[9] Specifically, the NC1 domain of COL7 binds with high affinity to the β3 chain of laminin332.[10] In this context, we can speculate that COL7 deficiency results in loss of intact binding between COL7 and laminin332, which might lead to disturbed regulation of ameloblast differentiation by laminin332. This disturbed regulation may cause abnormal ameloblast differentiation and enamel

defects in the COL7-deficient RDEB model mice and RDEB patients.

It is known that heterozygous carriers of the *LAMB3* defect and some with *COL17A1* defects display dental enamel defects, whereas those with *COL7A1* defects do not show these.[17,34] Similarly, in the present study, heterozygous mice carrying *Col7a1* defects (*Col7a1*$^{+/-}$ mice) showed no apparent tooth abnormalities. These facts suggest that haploinsufficiency of COL7 does not cause dental enamel defects. Therefore, a certain deficiency level of COL7 (more than 50% reduction of COL7) may be required to cause enamel abnormality.

Our results show that disruption of the *Col7a1* gene leads to insufficient interaction between enamel epithelium and the underlying mesenchyme via the EMJ, resulting in defective ameloblast differentiation. Consequently, the *Col7a1*$^{-/-}$ mice exhibit ameloblasts with malformed Tomes' processes and diminished secretion of enamel matrix at the secretary stage. We consider that these mechanisms contribute to the immature and irregular enamel formation seen in *Col7a1*$^{-/-}$ mice. Given these findings from the model mice in the present study, we speculate that the enamel structure in RDEB patients may be impaired and that this is why there is the greater risk of caries. In conclusion, epithelial–mesenchymal interactions via the EMJ are important for tooth morphogenesis, and anchoring fibrils consisting of COL7 are thought to be involved, via interaction between COL7 and laminin332, in the regulation of proliferation and differentiation of tooth-forming cells including ameloblasts.

Acknowledgments

We thank Mari Miura for her helpful discussion and oral treatment of the patient and Yoshiyuki Honma, Natsumi Ushijima, Yuko Hayakawa, and Kaori Sakai for their technical assistance.

References

1. Maas R, Bei M: The genetic control of early tooth development. Crit Rev Oral Biol Med 1997, 8:4–39
2. Liu F, Chu EY, Watt B, Zhang Y, Gallant NM, Andl T, Yang SH, Lu MM, Piccolo S, Schmidt-Ullrich R, Taketo MM, Morrisey EE, Atit R, Dlugosz AA, Millar SE: Wnt/beta-catenin signaling directs multiple stages of tooth morphogenesis. Dev Biol 2008, 313:210–224
3. Natsuga K, Shinkuma S, Nishie W, Shimizu H: Animal models of epidermolysis bullosa. Dermatol Clin 2010, 28:137–142
4. Asaka T, Akiyama M, Domon T, Nishie W, Natsuga K, Fujita Y, Abe R, Kitagawa Y, Shimizu H: Type XVII collagen is a key player in tooth enamel formation. Am J Pathol 2009, 174:91–100
5. Ryan MC, Lee K, Miyashita Y, Carter WG: Targeted disruption of the LAMA3 gene in mice reveals abnormalities in survival and late stage differentiation of epithelial cells. J Cell Biol 1999, 145:1309–1323
6. Fine JD, Eady RA, Bauer EA, Bauer JW, Bruckner-Tuderman L, Heagerty A, Hintner H, Hovnanian A, Jonkman MF, Leigh I, McGrath JA, Mellerio JE, Murrell DF, Shimizu H, Uitto J, Vahlquist A, Woodley D, Zambruno G: The classification of inherited epidermolysis bullosa (EB): report of the Third International Consensus Meeting on Diagnosis and Classification of EB. J Am Acad Dermatol 2008, 58:931–950
7. Tidman MJ, Eady RA: Evaluation of anchoring fibrils and other components of the dermal-epidermal junction in dystrophic epidermolysis bullosa by a quantitative ultrastructural technique. J Invest Dermatol 1985, 84:374–377
8. Sakai L, Keene D, Morris N, Burgeson R: Type VII collagen is a major structural component of anchoring fibrils. J Cell Biol 1986, 103:1577–1586
9. Rousselle P, Keene DR, Ruggiero F, Champliaud M-F, van der Rest M, Burgeson RE: Laminin 5 binds the NC-1 domain of type VII collagen. J Cell Biol 1997, 138:719–728
10. Chen M, Marinkovich MP, Jones JC, O'Toole EA, Li YY, Woodley DT: NC1 domain of type VII collagen binds to the beta3 chain of laminin 5 via a unique subdomain within the fibronectin-like repeats. J Invest Dermatol 1999, 112:177–183
11. Christiano A, Greenspan D, Hoffman G, Hoffman G, Zhang X, Tamai Y, Lin A, Dietz H, Hovnanian A, Uitto J: A missense mutation in type VII collagen in two affected siblings with recessive dystrophic epidermolysis bullosa. Nat Genet 1993, 4:62–66
12. Wright JT: Oral manifestations in the epidermolysis bullosa spectrum. Dermatol Clin 2010, 28:159–164
13. Harris JC, Bryan RA, Lucas VS, Roberts GJ: Dental disease and caries related microflora in children with dystrophic epidermolysis bullosa. Pediatr Dent 2001, 23:438–443
14. Kirkham J, Robinson C, Strafford SM, Bonass WA, Brookes SJ, Wright JT: The chemical composition of tooth enamel in recessive dystrophic epidermolysis bullosa: significance with respect to dental caries. J Dent Res 1996, 75:1672–1678
15. Wright JT, Fine JD, Johnson LB: Developmental defects of enamel in humans with hereditary epidermolysis bullosa. Archs Oral Biol 1993, 38:945–955
16. Shah H, McDonald F, Lucas V, Ashley P, Roberts G: A cephalometric analysis of patients with recessive dystrophic epidermolysis bullosa. Angle Orthod 2002, 72:55–60
17. Murrell DF, Pasmooij AM, Pas HH, Marr P, Klingberg S, Pfendner E, Uitto J, Sadowski S, Collins F, Widmer R, Jonkman MF: Retrospective diagnosis of fatal BP180-deficient non-Herlitz junctional epidermolysis bullosa suggested by immunofluorescence (IF) antigen-mapping of parental carriers bearing enamel defects. J Invest Dermatol 2007, 127:1772–1775
18. Heinonen S, Männikkö M, Klement JF, Whitaker-Menezes D, Murphy GF, Uitto J: Targeted inactivation of the type VII collagen gene (Col7a1) in mice results in severe blistering phenotype: a model for recessive dystrophic epidermolysis bullosa. J Cell Sci 1999, 112:3641–3648
19. Thesleff I, Partanen AM, Vainio S: Epithelial-mesenchymal interactions in tooth morphogenesis: the roles of extracellular matrix, growth factors, and cell surface receptors. J Craniofac Genet Dev Biol 1991, 11:229–237
20. Sawamura D, Goto M, Yasukawa K, Sato-Matsumura K, Nakamura H, Ito K, Nakamura H, Tomita Y, Shimizu H: Genetic studies of 20 Japanese families of dystrophic epidermolysis bullosa. J Hum Genet 2005, 50:543–546
21. Ito K, Sawamura D, Goto M, Nakamura H, Nishie W, Sakai K, Natsuga K, Shinkuma S, Shibaki A, Uitto J, Denton CP, Nakajima O, Akiyama M, Shimizu H: Keratinocyte-/fibroblast-targeted rescue of Col7a1-disrupted mice and generation of an exact dystrophic epidermolysis bullosa model using a human COL7A1 mutation. Am J Pathol 2009, 175:2508–2517
22. Shimizu H, Ishiko A, Masunaga T, Kurihara Y, Sato M, Bruckner-Tuderman L, Nishikawa T: Most anchoring fibrils in human skin originate and terminate in the lamina densa. Lab Invest 1997, 76:753–763
23. Fukumoto S, Kiba T, Hall B, Iehara N, Nakamura T, Longenecker G, Krebsbach PH, Nanci A, Kulkarni AB, Yamada Y: Ameloblastin is a cell adhesion molecule required for maintaining the differentiation state of ameloblasts. J Cell Biol 2004, 167:973–983
24. Fukumoto S, Yamada A, Nonaka K, Yamada Y: Essential roles of ameloblastin in maintaining ameloblast differentiation and enamel formation. Cells Tissues Organs 2005, 181:189–195
25. Masuya H, Shimizu K, Sezutsu H, Sakuraba Y, Nagano J, Shimizu A, Fujimoto N, Kawai A, Miura I, Kaneda H, Kobayashi K, Ishijima J, Maeda T, Gondo Y, Noda T, Wakana S, Shiroishi T: Enamelin (Enam) is essential for amelogenesis: eNU-induced mouse mutants as models for different clinical subtypes of human amelogenesis imperfecta (AI). Hum Mol Genet 2005, 14:575–583
26. Uitto J, Pulkkinen L, Christiano AM: Molecular basis of the dystrophic and junctional forms of epidermolysis bullosa: mutations in the type VII collagen and kalinin (laminin 5) genes. J Invest Dermatol 1994, 103:39S–46S

27. Christiano AM, Anhalt G, Gibbons S, Bauer EA, Uitto J: Premature termination codons in the type VII collagen gene (COL7A1) underlie severe, mutilating recessive dystrophic epidermolysis bullosa. Genomics 1994, 21:160–168
28. Miletich I, Sharpe PT: Normal and abnormal dental development. Hum Mol Genet 2003, 12:R69–R73
29. Fleischmannova J, Matalova E, Tucker AS, Sharpe PT: Mouse models of tooth abnormalities. Eur J Oral Sci 2008, 116:1–10
30. Slavkin HC: Regulatory issues during early craniofacial development: a summary. Cleft Palate J 1990, 27:101–109
31. Smith CE: Cellular and chemical events during enamel maturation. Crit Rev Oral Biol Med 1998, 9:128–161
32. Bartlett JD, Skobe Z, Lee DH, Wright JT, Li Y, Kulkarni AB, Gibson CW: A developmental comparison of matrix metalloproteinase-20 and amelogenin null mouse enamel. Eur J Oral Sci 2006, 114:18–23
33. Morotomi T, Kawano S, Toyono T, Kitamura C, Terashita M, Uchida T, Toyoshima K, Harada H: In vitro differentiation of dental epithelial progenitor cells through epithelial-mesenchymal interactions. Arch Oral Biol 2005, 50:695–705
34. McGrath JA, Gatalica B, Li K, Dunnill MG, McMillan JR, Christiano AM, Eady RA, Uitto J: Compound heterozygosity for a dominant glycine substitution and a recessive internal duplication mutation in the type XVII collagen gene results in junctional epidermolysis bullosa and abnormal dentition. Am J Pathol 1996, 148:1787–96

nature genetics

Haploinsufficiency for *AAGAB* causes clinically heterogeneous forms of punctate palmoplantar keratoderma

Elizabeth Pohler[1], Ons Mamai[2,3], Jennifer Hirst[4], Mozheh Zamiri[5], Helen Horn[6], Toshifumi Nomura[7], Alan D Irvine[8,9], Benvon Moran[8], Neil J Wilson[1], Frances J D Smith[1], Christabelle S M Goh[1], Aileen Sandilands[1], Christian Cole[1,10], Geoffrey J Barton[10], Alan T Evans[11], Hiroshi Shimizu[7], Masashi Akiyama[12], Mitsuhiro Suehiro[13], Izumi Konohana[14], Mohammad Shboul[3], Sebastien Teissier[3], Lobna Boussofara[15], Mohamed Denguezli[15], Ali Saad[2], Moez Gribaa[2], Patricia J Dopping-Hepenstal[16], John A McGrath[17], Sara J Brown[1], David R Goudie[18], Bruno Reversade[3,19], Colin S Munro[20] & W H Irwin McLean[1]

© 2012 Nature America, Inc. All rights reserved.

Palmoplantar keratodermas (PPKs) are a group of disorders that are diagnostically and therapeutically problematic in dermatogenetics[1–3]. Punctate PPKs are characterized by circumscribed hyperkeratotic lesions on the palms and soles with considerable heterogeneity. In 18 families with autosomal dominant punctate PPK, we report heterozygous loss-of-function mutations in *AAGAB*, encoding α- and γ-adaptin–binding protein p34, located at a previously linked locus at 15q22. α- and γ-adaptin–binding protein p34, a cytosolic protein with a Rab-like GTPase domain, was shown to bind both clathrin adaptor protein complexes, indicating a role in membrane trafficking. Ultrastructurally, lesional epidermis showed abnormalities in intracellular vesicle biology. Immunohistochemistry showed hyperproliferation within the punctate lesions. Knockdown of *AAGAB* in keratinocytes led to increased cell division, which was linked to greatly elevated epidermal growth factor receptor (EGFR) protein expression and tyrosine phosphorylation. We hypothesize that p34 deficiency may impair endocytic recycling of growth factor receptors such as EGFR, leading to increased signaling and cellular proliferation.

Palmoplantar keratoderma (MIM 148600) describes a group of hereditary skin disorders characterized by thickening (hyperkeratosis) of the epidermis of the palms and soles[1]. Historically, PPKs have been classified according to the pattern of lesions (diffuse, focal, punctate and striate), as well as by histopathological changes (epidermolytic, non-epidermolytic and porokeratotic). Molecular genetics now allows for improved classification and diagnosis and for personalized approaches to treatment. Three distinct types of inherited punctate PPK are recognized by Online Mendelian Inheritance in Man (OMIM)[2]: PPKP1 (also known as the Buschke-Fischer-Brauer type; MIM 148600), for which the associated locus mapped to 15q22 (refs. 4–6); PPKP2 (porokeratotic type; MIM 175860), for which no locus has been mapped yet; and PPKP3 (also known as acrokeratoelastoidosis; MIM 101850), for which preliminary linkage suggests a possible associated locus at 2p25–p12 (ref. 7). An additional disease-associated locus was identified at 8q24.13–8q24.21 in two Chinese families whose phenotypes resemble PPKP1 clinically and histologically[8]. Here we studied a collection of 18 kindreds with PPKP1 from Scotland, Ireland, Japan and Tunisia, 11 of whom had a family history consistent with autosomal dominant inheritance (**Supplementary Fig. 1**). In our PPKP1 case collection, there was considerable phenotypic variation (**Fig. 1**). In all families, onset was typically during the first to second decade of life, with the appearance of small circumscribed lesions on the palms and soles. These lesions consistently increased in number with advancing age and coalesced later to form larger lesions. In some families, lesions remained subtle (**Fig. 1a,b**), whereas the phenotype in other families, resembling human papilloma virus (HPV)-induced papilloma-like lesions, was much more severe, painful and debilitating (**Fig. 1c,d**). Histology of lesional palmar epidermis from three unrelated kindreds (families 1,

[1]Centre for Dermatology and Genetic Medicine, College of Life Sciences and College of Medicine, Dentistry & Nursing, University of Dundee, Dundee, UK. [2]Laboratory of Human Cytogenetics, Molecular Genetics and Reproductive Biology, Farhat Hached University Hospital, Sousse, Tunisia. [3]Institute of Medical Biology, Agency for Science, Technology and Research (A*STAR), Singapore. [4]Cambridge Institute for Medical Research, University of Cambridge, Cambridge, UK. [5]Department of Dermatology, University Hospital Crosshouse, Kilmarnock, UK. [6]Department of Dermatology, Royal Infirmary of Edinburgh, Edinburgh, UK. [7]Department of Dermatology, Hokkaido University Graduate School of Medicine, Sapporo, Japan. [8]Department of Paediatric Dermatology, Our Lady's Children's Hospital, Dublin, Ireland. [9]Institute for Molecular Medicine, Trinity College Dublin, Dublin, Ireland. [10]Bioinformatics Research Group, Division of Biochemistry and Drug Discovery, College of Life Sciences, University of Dundee, Dundee, UK. [11]Department of Pathology, Ninewells Hospital and Medical School, Dundee, UK. [12]Department of Dermatology, Nagoya University Graduate School of Medicine, Nagoya, Japan. [13]Department of Dermatology, Otsu Municipal Hospital, Otsu, Japan. [14]Department of Dermatology, Hiratsuka Municipal Hospital, Hiratsuka, Japan. [15]Department of Dermatology and Venerology, Farhat Hached University Hospital, Sousse, Tunisia. [16]Guy's and St. Thomas' (GSTS) Pathology, St. Thomas' Hospital, London, UK. [17]St. John's Institute of Dermatology, King's College London, London, UK. [18]Human Genetics Unit, Ninewells Hospital and Medical School, Dundee, UK. [19]Department of Paediatrics, National University of Singapore, Singapore. [20]Department of Dermatology, Southern General Hospital, Glasgow, UK. Correspondence should be addressed to W.H.I.M. (w.h.i.mclean@dundee.ac.uk).

Received 5 July; accepted 21 September; published online 14 October 2012; doi:10.1038/ng.2444

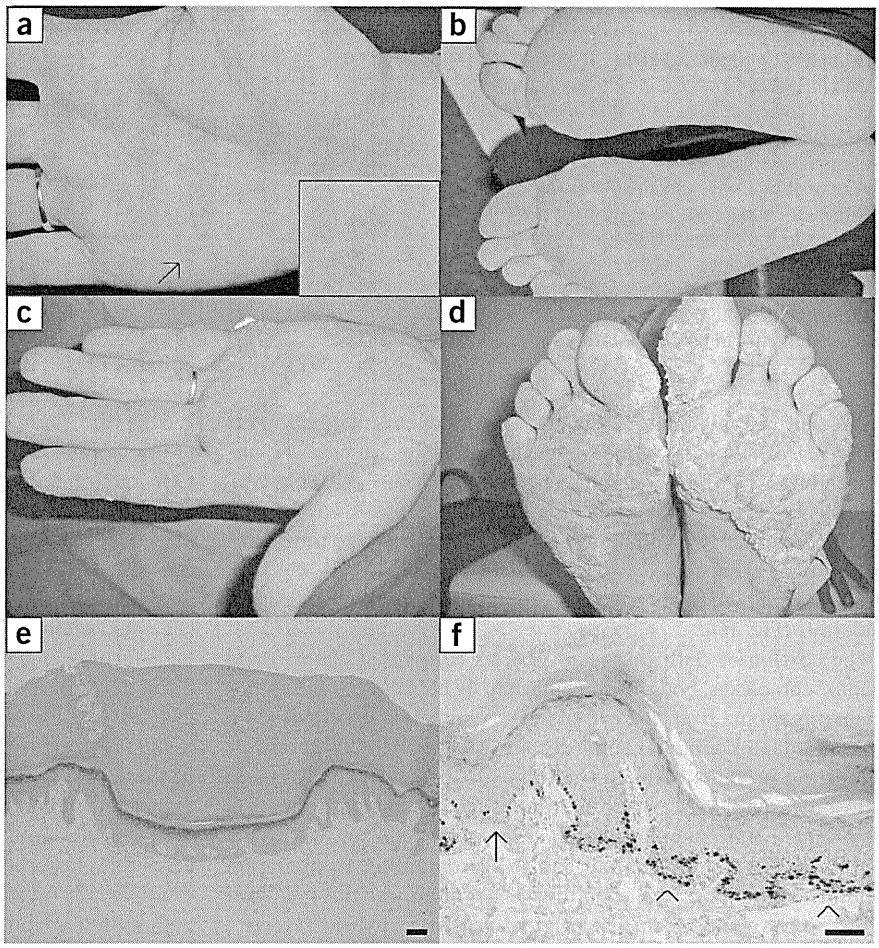

Figure 1 Clinical and histological features of punctate PPK. (**a**) The palm of the proband in family 1 with PPKP1 shows numerous small, hard, slightly indented hyperkeratotic lesions (arrow). Inset, magnified view of the lesion indicated by the arrow. (**b**) On the soles, lesions tend to coalesce at pressure points, and the presentation can therefore resemble a focal form of keratoderma. (**c**,**d**) In some cases, the phenotype is much more severe, as seen with the hand (**c**) and feet (**d**) of the proband from family 15. (**e**) Hematoxylin and eosin staining of a section showing a punch sample of skin incorporating a well-defined central epidermal depression associated with hypergranulosis and a prominent layer of overlying orthokeratosis. Scale bar, 500 μm. (**f**) Staining for the proliferation marker Ki67 highlights an increase in the number of keratinocytes in the cell cycle within the floor of the epidermal depression (arrowheads) compared to perilesional epidermis (arrow). Scale bar, 100 μm.

11 and 15) all showed very similar findings of a well-defined central epidermal depression associated with hypergranulosis and a prominent layer of overlying orthokeratosis (**Fig. 1e**). Immunohistochemical staining for the cell proliferation marker Ki67 showed continuous staining of the basal cell (proliferative) compartment of the epidermis beneath the hyperkeratotic lesions (**Fig. 1f**), indicative of a hyperproliferative form of hyperkeratosis rather than a retention hyperkeratosis due to defective desquamation.

Microsatellite linkage to the previously reported 15q22 locus was observed in a large Tunisian kindred originating from Saudi Arabia (**Supplementary Fig. 2**), with a maximum two-point logarithm of odds (LOD) score of 8.18 at recombination frequency (θ) = 0 obtained for D15S983 (**Supplementary Table 1**). The family was reported previously[9]. A 6.24-Mb key interval containing 80 RefSeq genes was defined by visible recombination with markers D15S993 (proximal) and D15S977 (distal). This locus overlaps the previously reported intervals associated with PPKP1 (**Supplementary Table 2**). In parallel, the proband in family 1 (of Scottish ancestry) was subjected to whole-exome sequencing. Of the 28,513 SNPs identified, we elected to concentrate on loss-of-function variants located within the key interval defined by our linkage data and that previously reported. Of 106 unique stop-gain SNPs in the exome data set, only 3 SNPs, all heterozygous in the proband, were located on chromosome 15 (**Supplementary Table 3**). Two were located well outside the interval, including a known SNP, rs57809907, in *DYX1C1*, c.1617C>T, predicted to cause a p.Glu417* alteration, and a second previously unreported variant of unknown consequence in *GABRG3*, c.1316T>A, predicted to cause a p.Leu439* alteration. The remaining variant, c.481C>T in *AAGAB*, predicted to cause a p.Arg161* alteration (mRNA, NM_024666; protein, NP_078942), fell within our linkage interval and that initially reported[5] but was just outside the interval reported in a Chinese kindred[6]. This variant was absent from current dbSNP and 1000 Genomes Project data sets (1 June 2012). The mutation was confirmed by conventional sequencing and cosegregated with the PPKP1 phenotype in family 1 (**Supplementary Fig. 3a**,**b**). By conventional sequencing, a second loss-of-function mutation, c.346_347delAG, was identified and found to fully cosegregate with disease in the linked kindred and two additional Tunisian families (**Supplementary Fig. 3c**,**d**). Sequencing of the remaining 16 families identified a total of 8 mutations in *AAGAB* (2 nonsense, 5 frameshift and 1 splice-site mutation, as detailed in **Supplementary Table 4**). *AAGAB*, consisting of ten exons spanning 53,708 bp of genomic DNA, encodes α- and γ-adaptin–binding protein p34, which was identified in a yeast two-hybrid screen using a subunit of the adapter protein (AP)-1 complex as bait[10]. The positions of the predicted alterations in relation to the protein organization of p34 are shown (**Fig. 2**).

Conventional RT-PCR showed expression in palmoplantar epidermis comparable to that in abdominal skin (data not shown). By quantitative RT-PCR (qRT-PCR), we confirmed that *AAGAB* is expressed at broadly comparable levels in skin, HeLa cells, primary epidermal keratinocytes and the commonly used keratinocyte cell line, HaCaT[11] (**Fig. 3a**). Using qRT-PCR, we also showed that *AAGAB* message is very widely expressed across tissues, including

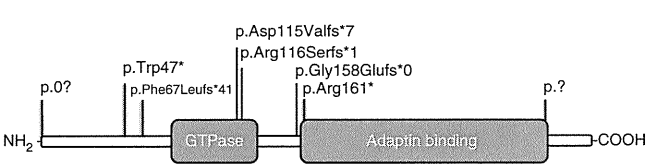

Figure 2 Identification of mutations in *AAGAB* in families with PPKP1. Protein domain organization of the p34 protein encoded by *AAGAB*, showing the positions of all eight alterations identified. Further details on the mutations are provided in **Supplementary Table 4**. Examples of sequence traces are shown in **Supplementary Figure 3**.

© 2012 Nature America, Inc. All rights reserved.

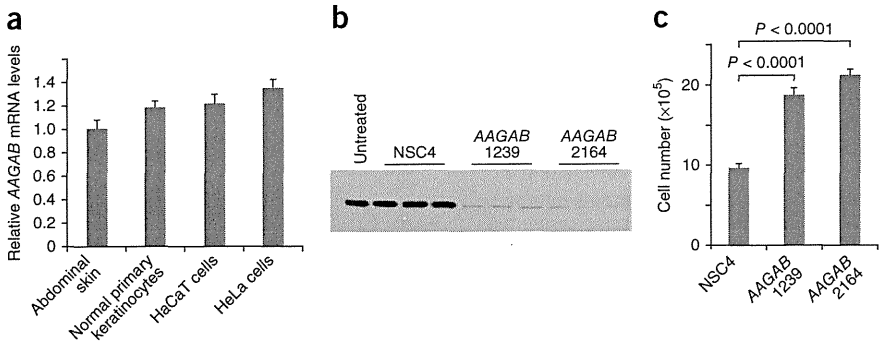

Figure 3 *AAGAB* is expressed in skin and keratinocytes and its depletion leads to increased cell numbers over time. (**a**) qRT-PCR showed that *AAGAB* mRNA is expressed in skin and is present at broadly comparable levels in primary epidermal keratinocytes. HeLa cells and the epidermal keratinocyte cell line HaCaT. (**b**) Protein blot showing that two independent siRNAs (designated *AAGAB* 1239 and 2164) potently lower p34 expression in HaCaT cells. NSC4, nonspecific control siRNA (inverted *lacZ* sequence). (**c**) *AAGAB* knockdown by either siRNA leads to an approximate twofold increase in HaCaT cell division 96 h after transfection. Error bars, s.d.

in the skin (**Supplementary Fig. 4**). Two independent small interfering RNAs (siRNAs) were developed that resulted in almost complete reduction of the amount of p34 protein in HaCaT cells (**Fig. 3b**). Treatment of HaCaT cells with either of these potent siRNAs resulted in an approximately twofold increase in cell number over time compared to cells transfected with a negative control siRNA (**Fig. 3c**), thus mirroring the high epidermal proliferation observed in lesional epidermis (**Fig. 1f**).

The coating of clathrin-coated vesicles consists of clathrin and adaptor complexes, both of which have to be recruited to the appropriate membrane from the cytoplasm[12,13]. The two most abundant types of adaptor protein complexes are AP-1, which is responsible for sorting proteins between the trans-Golgi network (TGN) and endosomes, and AP-2, which is responsible for sorting proteins at the plasma membrane. Both are heterotypic complexes, with AP-1 containing a γ-adaptin subunit and AP-2 containing an α-adaptin subunit. Although cDNA encoding p34 protein was the predominant species cloned from the original yeast two-hybrid screen[10], difficulty in obtaining antibodies specific to the p34 protein meant that further biochemical confirmation of these protein-protein interactions were not presented. Here, using two independent antibodies to p34 that were made in house, we confirmed by immunoprecipitation combined with protein blotting that this protein indeed interacts with both AP-1 and AP-2 complexes in the cytosol (**Fig. 4a**). Cytosolic localization was confirmed by immunocytochemistry using constructs encoding p34 fused to green fluorescent protein (GFP) at either the N or C terminus (**Fig. 4b**), although fusion of GFP at the C terminus also led to some nuclear accumulation of the fusion protein. Cell fractionation studies showed that p34 protein is found in the cytosol but not in the membrane or clathrin-coated vesicle fractions in HeLa cells (**Fig. 4c**). Almost complete siRNA-mediated knockdown of *AAGAB* (**Fig. 4d**) did not lead to an obvious change in the plasma membrane or TGN localization of AP-2 or AP-1, respectively (**Fig. 4e**). Neither AP-1 nor AP-2 colocalized with the N- or C-terminal GFP fusions of p34 (**Supplementary Fig. 5**). Essentially identical diffuse cytoplasmic localization data were obtained in the keratinocyte cell line HaCaT (data not shown). Overall, these data confirm that p34 is a cytosolic protein that binds to AP-1 and AP-2; however, p34 does not follow these protein complexes into their membrane-associated vesicle populations on intracellular membranes or at the plasma membrane, respectively. This finding is consistent with a possible chaperone function for p34, as previously suggested[10]. For example, p34 might either prevent soluble clathrin from assembling with soluble adaptor complexes in the cytosol, be involved in vesicle uncoating or aid recruitment of soluble adaptors to membranes[10]. Bioinformatics analysis identified a GTPase domain in p34, which is most closely related to the Rab superfamily of vesicular trafficking proteins (**Fig. 2** and **Supplementary Fig. 6**). It is not known whether this GTPase domain is functional. If this is the case, our finding may be indicative of a role for p34 in the active transport of cytosolic adaptor complexes rather than a more passive chaperone function[14].

Ultrastructural analysis of lesional plantar skin showed mild acanthosis, a reduction in the granular cell layer and compact orthokeratosis (**Supplementary Fig. 7**). In basal keratinocytes (**Fig. 5**), there was a large increase in the number of small vesicles

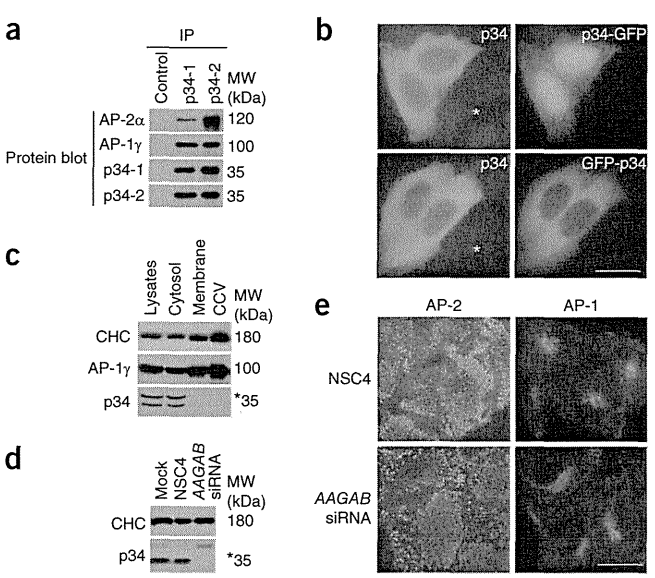

Figure 4 p34 associates with AP-1 and AP-2 in the cytosol. (**a**) Native immunoprecipitation of HeLa cytosolic extracts was performed with antibodies against p34, α-adaptin (detecting the AP-2 complex) and γ-adaptin (detecting the AP-1 complex). (**b**) HeLa cells were transiently transfected with constructs encoding p34 fused with GFP either at the C terminus (p34-GFP) or N terminus (GFP-p34). Both fusion proteins show a mainly cytosolic localization, consistent with the staining pattern (albeit faint) observed using antibody against p34 in either transfected or untransfected cells (*). (**c**) HeLa cell lysates were subjected to fractionation into cytosol, membrane and clathrin-coated vesicle (CCV) fractions, and protein blot analysis was performed for clathrin heavy chain (CHC), AP-1 and p34. *, cross-reacting band. (**d**) HeLa cells were treated with siRNA (SMARTpool, Thermo-Fisher) to reduce expression of p34, and protein blot analysis was performed for CHC and p34. *, cross-reacting band. The amount of p34 protein was reduced by >95% in cells transfected with *AAGAB* siRNA. (**e**) Localization of AP-1 and AP-2 visualized by immunofluorescence after knockdown of *AAGAB*. AP-2–containing membrane-associated vesicles and AP-1–TGN appear unperturbed. Scale bars, 20 μm.

© 2012 Nature America, Inc. All rights reserved.

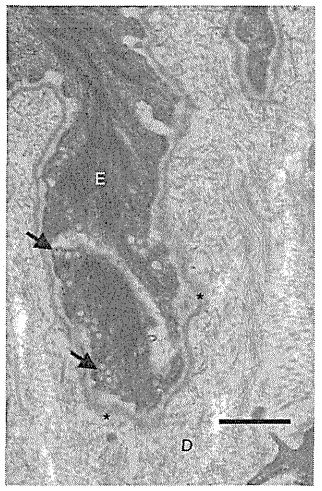

Figure 5 Transmission electron microscopy of lesional plantar skin shows vesicle abnormalities within basal keratinocytes. Transmission electron microscopy of a basal epidermal keratinocyte (E) within PPKP1 lesional epidermis shows an abnormal abundance of membrane-bound vesicles abutting the plasma membrane (arrows), close to the cutaneous basement membrane (*). D, dermis. Scale bar, 0.2 μm. Additional electron micrographs are shown in **Supplementary Figure 7**.

close to the cell membrane and prominent dilatation of the Golgi apparatus in lesional epidermis compared to normal, control skin (**Supplementary Fig. 7**). These ultrastructural features are consistent with a defect in vesicle transport.

We hypothesized that a mechanism whereby perturbation of vesicle trafficking could lead to increased epidermal proliferation might involve recycling of EGFR. EGFR is known to undergo rapid turnover in a process that requires a number of sorting steps, including clathrin- and AP-2–dependent endocytosis[15,16]. Internalized ligand-bound EGFR is either shuttled to late endosomes/lysosomes for degradation or into recycling endosomes, where, after removal of the bound ligand and dephosphorylation, the receptor is returned to the plasma membrane via vesicle fusion. Knockdown of *AAGAB* in HaCaT cells led to a modest ~2.5-fold increase in *EGFR* mRNA levels relative to cells transfected with control siRNA, as determined by qRT-PCR (data not shown); however, the amount of total EGFR protein was >10-fold higher in protein blot analysis (**Fig. 6a**), consistent with decreased EGFR turnover. Notably, phosphorylation of EGFR at Tyr992, indicating active EGFR signaling[17], was increased by >20-fold in cells with *AAGAB* knockdown (**Fig. 6b**). The regulation of EGFR signaling via clathrin-mediated endocytosis is a complex process mediated by Rab proteins[15], dynamin[18], AP-2 and the Grb2 adaptor protein that involves multiple mechanisms relating to post-translational modification of the receptor itself[19]. Disruption of EGFR endocytosis by double knockout of the *Dnm1* and *Dnm2* genes encoding the motor proteins dynamin-1 and dynamin-2, respectively, in mouse has been shown to result in decreased protein turnover with increased EGFR signaling[18], very similar to what we observed with knockdown of *AAGAB*.

Here, using a combination of genetic linkage analysis and whole-exome sequencing, we have identified mutations in the *AAGAB* gene, encoding p34, that cause the autosomal dominant form of punctate PPK that was previously linked to 15q22 known as PPKP1 (MIM 148600)[5,6,9]. AP-2 is known to be involved in EGFR endocytosis[19], and we confirmed here that p34 binds cytosolic AP-2 (**Fig. 4**) and show that p34 deficiency results in increased epidermal cell proliferation (**Fig. 1f** and **Fig. 3**). Overall, p34 seems to have a hitherto unrecognized role in the control of cell division, possibly by contributing to normal endocytic recycling of receptor tyrosine kinases, such as EGFR[15,16,18,19]. Other genes involved in intracellular vesicle trafficking have been linked to inherited skin diseases where hyperkeratosis and/or keratoderma form part of the phenotypic constellation. These genes include *SNAP29* in cerebral dysgenesis, neuropathy, ichthyosis and keratoderma (CEDNIK) syndrome[20] and *VPS33B* in arthrogryposis, renal dysfunction and cholestasis (ARC) syndrome[21], both of which encode proteins required for vesicle membrane fusion in the epidermis and other tissues. Moreover, loss-of-function mutations in *AP1S1*, which encodes the small σ1A subunit of the AP-1 complex, have been shown to cause the recessive neurocutaneous disorder mental retardation, enteropathy, deafness, peripheral neuropathy, ichthyosis and keratodermia (MEDNIK)[22]. Similarly, defects in multiple proteins involved in melanosome transport and fusion lead to the pigmentation disorder Griscelli syndrome[23], and mutations in the gene encoding the AP-3 subunit protein β3A have been linked to Hermansky-Pudlak syndrome type 2, which consists of oculocutaneous albinism and other features[24]. Thus, mutations in a growing number of genes involved in vesicle transport have been linked to genetic skin disease, with or without extracutaneous phenotypes.

Disruption of EGFR signaling is a feature of neoplasia. There are anecdotal reports of cancer occurring in association with punctate PPK[25]; however, without genetic testing, we cannot determine whether the *AAGAB* gene was involved in those cases. Although a few cases of cancer were reported in the larger families studied here, we did not observe cosegregation with the *AAGAB* mutations, and, therefore, any causal link between *AAGAB* mutations and cancer remains unproven.

It remains unclear why haploinsufficiency for this widely expressed gene leads to a phenotype limited to palm and sole epidermis, although this is not unusual in hereditary skin disease. For example, haploinsufficiency for the *DSP* or *DSG1* genes encoding the desmosomal proteins desmoplakin and desmoglein-1, respectively (refs. 26,27), both of which are structural proteins expressed throughout the epidermis, lead to striate palmoplantar keratoderma[28]. Another unanswered question relates to why the hyperkeratotic lesions are focal. These lesions are late in onset, appearing in the first or second decade of life, and increase in number with advancing age. This pattern of appearance might be explained by a 'second hit' mutation in *AAGAB*, and we therefore sequenced the gene using genomic DNA derived from microdissected lesional tissue from more than one affected individual. We found neither loss of heterozygosity nor a

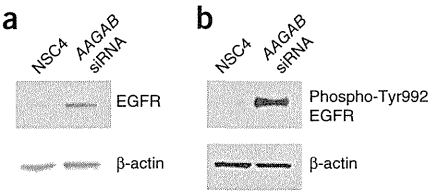

Figure 6 Knockdown of *AAGAB* greatly increases EGFR protein expression. (**a**) Knockdown of *AAGAB* with siRNA 1239 leads to greatly increased EGFR protein expression relative to cells transfected with NSC4. Part of the blot was stained for β-actin for a loading control and to normalize EGFR quantification. Using the LI-COR Odyssey system, the observed upregulation of EGFR was found to be greater than tenfold. (**b**) Knockdown of *AAGAB* with siRNA 1239 also leads to greatly increased phosphorylation of Tyr992 on the EGFR protein compared to transfection with NSC4. Using the LI-COR Odyssey system, the observed increase in phosphorylation of this residue was found to be >20-fold.

© 2012 Nature America, Inc. All rights reserved.

second compound heterozygous *AAGAB* mutation (data not shown). We also attempted immunohistochemistry; however, neither the in-house nor commercially available antibody to p34 gave a signal on fixed abdominal tissue from a normal control. It is also possible that a second somatic mutation might occur in a gene other than *AAGAB*.

In conclusion, this study expands the molecular diagnostic repertoire for keratodermas and shows that the p34 protein, which is associated with AP-1 and AP-2, is involved in regulating epidermal cell division.

URLs. The Eastern Sequence and Informatics Hub (EASIH), http://www.easih.ac.uk/; Pachyonychia Congenita Project, http://www.pachyonychia.org/.

METHODS

Methods and any associated references are available in the online version of the paper.

Note: Supplementary information is available in the online version of the paper.

ACKNOWLEDGMENTS

The authors dedicate this paper to their erstwhile colleague, the late dermatologist and cell biologist Susan M. Morley, who treated some of the individuals studied here. We thank M. Robinson and C. Watts for insightful discussions, I. Nathke and I. Newton for their help with protein blot quantification and Tayside Tissue Bank, Dundee for providing skin samples. Specialist Sequencing and Bioinformatics Services were provided by The Eastern Sequence and Informatics Hub (EASIH) at the University of Cambridge, which is supported by the National Institute for Health Research and the Cambridge Biomedical Research Centre. This work was supported by a Wellcome Trust Programme Grant (092530/Z/10/Z) to W.H.I.M., A.D.I. and G.J.B., a Wellcome Trust Strategic Award (098439/Z/12/Z) to W.H.I.M., G.J.B. and J.A.M., a project grant from the Pachyonychia Congenita Project to F.J.D.S. and a strategic positioning fund for Genetic Orphan Diseases from A*STAR. O.M. was funded by an A*STAR Research Attachment Program (ARAP), and B.R. is a fellow of the Branco Weiss Foundation.

AUTHOR CONTRIBUTIONS

W.H.I.M. designed the study. M.Z., H.H., T.N., A.D.I., B.M., H.S., M.A., M. Suehiro, I.K., L.B., M.D., A. Saad, M.G., O.M. and C.S.M. diagnosed subjects and collected clinical samples and phenotype data. E.P., O.M., N.J.W., M. Shboul and S.T. conducted genotyping, mapping and sequencing. J.H. and E.P. performed protein functional studies. J.H. generated the polyclonal antibodies to p34. C.C. and G.J.B. carried out next-generation sequencing bioinformatics. A.T.E. performed the dermatopathology analysis. P.J.D.-H. and J.A.M. performed ultrastructural analysis. S.J.B., O.M. and A. Sandilands provided tissue samples. C.S.M.G. and A. Sandilands performed the tissue expression analysis. D.R.G. performed statistical genetics. W.H.I.M., E.P., J.H., B.R., J.A.M., C.S.M. and F.J.D.S. wrote the manuscript.

COMPETING FINANCIAL INTERESTS

The authors declare no competing financial interests.

Published online at http://www.nature.com/doifinder/10.1038/ng.2444.
Reprints and permissions information is available online at http://www.nature.com/reprints/index.html.

1. Itin, P.H. & Fistarol, S.K. Palmoplantar keratodermas. *Clin. Dermatol.* **23**, 15–22 (2005).
2. Stevens, H.P. *et al.* Linkage of an American pedigree with palmoplantar keratoderma and malignancy (palmoplantar ectodermal dysplasia type III) to 17q24. Literature survey and proposed updated classification of the keratodermas. *Arch. Dermatol.* **132**, 640–651 (1996).
3. Kelsell, D.P. & Stevens, H.P. The palmoplantar keratodermas: much more than palms and soles. *Mol. Med. Today* **5**, 107–113 (1999).
4. Emmert, S. *et al.* 47 patients in 14 families with the rare genodermatosis keratosis punctata palmoplantaris Buschke-Fischer-Brauer. *Eur. J. Dermatol.* **13**, 16–20 (2003).
5. Martinez-Mir, A. *et al.* Identification of a locus for type I punctate palmoplantar keratoderma on chromosome 15q22-q24. *J. Med. Genet.* **40**, 872–878 (2003).
6. Gao, M. *et al.* Refined localization of a punctate palmoplantar keratoderma gene to a 5.06-cM region at 15q22.2–15q22.31. *Br. J. Dermatol.* **152**, 874–878 (2005).
7. Jung, E.G. Acrokeratoelastoidosis. *Humangenetik* **17**, 357–358 (1973).
8. Zhang, X.J. *et al.* Identification of a locus for punctate palmoplantar keratodermas at chromosome 8q24.13–8q24.21. *J. Invest. Dermatol.* **122**, 1121–1125 (2004).
9. El Amri, I. *et al.* Clinical and genetic characteristics of Buschke-Fischer-Brauer's disease in a Tunisian family. *Ann. Dermatol. Venereol.* **137**, 269–275 (2010).
10. Page, L.J., Sowerby, P.J., Lui, W.W. & Robinson, M.S. γ-synergin: an EH domain–containing protein that interacts with γ-adaptin. *J. Cell Biol.* **146**, 993–1004 (1999).
11. Boukamp, P. *et al.* Normal keratinization in a spontaneously immortalized aneuploid human keratinocyte cell line. *J. Cell Biol.* **106**, 761–771 (1988).
12. Robinson, M.S. & Bonifacino, J.S. Adaptor-related proteins. *Curr. Opin. Cell Biol.* **13**, 444–453 (2001).
13. Robinson, M.S. Adaptable adaptors for coated vesicles. *Trends Cell Biol.* **14**, 167–174 (2004).
14. Horgan, C.P. & McCaffrey, M.W. Rab GTPases and microtubule motors. *Biochem. Soc. Trans.* **39**, 1202–1206 (2011).
15. Ceresa, B.P. Regulation of EGFR endocytic trafficking by rab proteins. *Histol. Histopathol.* **21**, 987–993 (2006).
16. Rappoport, J.Z. & Simon, S.M. Endocytic trafficking of activated EGFR is AP-2 dependent and occurs through preformed clathrin spots. *J. Cell Sci.* **122**, 1301–1305 (2009).
17. Downward, J., Parker, P. & Waterfield, M.D. Autophosphorylation sites on the epidermal growth factor receptor. *Nature* **311**, 483–485 (1984).
18. Sousa, L.P. *et al.* Suppression of EGFR endocytosis by dynamin depletion reveals that EGFR signaling occurs primarily at the plasma membrane. *Proc. Natl. Acad. Sci. USA* **109**, 4419–4424 (2012).
19. Goh, L.K., Huang, F., Kim, W., Gygi, S. & Sorkin, A. Multiple mechanisms collectively regulate clathrin-mediated endocytosis of the epidermal growth factor receptor. *J. Cell Biol.* **189**, 871–883 (2010).
20. Sprecher, E. *et al.* A mutation in *SNAP29*, coding for a SNARE protein involved in intracellular trafficking, causes a novel neurocutaneous syndrome characterized by cerebral dysgenesis, neuropathy, ichthyosis, and palmoplantar keratoderma. *Am. J. Hum. Genet.* **77**, 242–251 (2005).
21. Gissen, P. *et al.* Mutations in *VPS33B*, encoding a regulator of SNARE-dependent membrane fusion, cause arthrogryposis–renal dysfunction–cholestasis (ARC) syndrome. *Nat. Genet.* **36**, 400–404 (2004).
22. Montpetit, A. *et al.* Disruption of *AP1S1*, causing a novel neurocutaneous syndrome, perturbs development of the skin and spinal cord. *PLoS Genet.* **4**, e1000296 (2008).
23. Van Gele, M., Dynoodt, P. & Lambert, J. Griscelli syndrome: a model system to study vesicular trafficking. *Pigment Cell Melanoma Res.* **22**, 268–282 (2009).
24. Tarpey, P.S. *et al.* Mutations in the gene encoding the Sigma 2 subunit of the adaptor protein 1 complex, *AP1S2*, cause X-linked mental retardation. *Am. J. Hum. Genet.* **79**, 1119–1124 (2006).
25. Bennion, S.D. & Patterson, J.W. Keratosis punctata palmaris et plantaris and adenocarcinoma of the colon. A possible familial association of punctate keratoderma and gastrointestinal malignancy. *J. Am. Acad. Dermatol.* **10**, 587–591 (1984).
26. Armstrong, D.K. *et al.* Haploinsufficiency of desmoplakin causes a striate subtype of palmoplantar keratoderma. *Hum. Mol. Genet.* **8**, 143–148 (1999).
27. Wan, H. *et al.* Striate palmoplantar keratoderma arising from desmoplakin and desmoglein 1 mutations is associated with contrasting perturbations of desmosomes and the keratin filament network. *Br. J. Dermatol.* **150**, 878–891 (2004).
28. McLean, W.H. Genetic disorders of palm skin and nail. *J. Anat.* **202**, 133–141 (2003).

© 2012 Nature America, Inc. All rights reserved.

ONLINE METHODS

Affected individuals and phenotypes. Individuals from 18 apparently unrelated families presented with PPK at dermatology clinics in Scotland, Ireland, Japan and Tunisia. Clinical examination and histological analysis of affected persons was consistent with a diagnosis of the Buschke-Fischer-Brauer type of punctate PPK (PPKP1; MIM 148600)[2]. In severely affected cases, where keratoderma resembled plantar warts, the presence of HPV was excluded in the clinical work-up. Blood samples were obtained in tubes containing the anticoagulant EDTA from the affected individuals with written informed consent and approval from the institutional ethics committee (Tayside Committee on Research Ethics, Dundee, UK) that complied with the Declaration of Helsinki Principles. DNA was extracted using standard procedures.

Linkage analysis. Microsatellite genotypes were generated for members of family 15 using standard protocols. LOD scores were calculated using FASTLINK[29,30], assuming a mutant allele frequency of 1 in 50,000. The LOD scores were recalculated assuming a 10% chance of non-penetrance because of difficulty in obtaining a definitive clinical ascertainment in some individuals in family 15 (the family resides in a remote mountainous area of Tunisia).

Exome sequencing. Exome enrichment was performed using the Agilent SureSelect 50Mb exome enrichment system, using the protocol for Applied Biosystems SOLiD (Protocol version 1.0, May 2010). Sequencing was then performed on the ABI SOLiD platform (Applied Biosystems), with an average sequencing depth of >30× across the exome. Next-generation sequencing and SNP calling were performed by The Eastern Sequence and Informatics Hub (EASIH; see URLs). To simplify filtering of the exome data, all SNP calls were put into a MySQL database and queried via an in-house web-based django front-end.

Histology. Routine hematoxylin and eosin staining of paraffin-embedded tissue was performed using standard protocols. Immunohistochemical staining for the cell proliferation marker Ki67 was performed using polyclonal antibody HPA000451 (Sigma-Aldrich).

Mutation analysis of the *AAGAB* gene. The individual exons of *AAGAB* were amplified by PCR using genomic primers (sequences listed in **Supplementary Table 5**) and the following cycling conditions: 1 cycle at 94 °C for 5 min; 35 cycles at 94 °C for 30 s, 55 °C for 30 s and 72 °C for 1 min; and 1 final extension at 72 °C for 5 min.

Cell culture. HaCaT keratinocytes were maintained in a monolayer in 5% CO_2 in DMEM (Invitrogen) supplemented with 10% FCS. Normal human keratinocytes were obtained from CELLnTECH and cultured in the defined growth medium CnT57 (TCS Cellworks). HeLa cells were cultured in DMEM supplemented with 10% FCS, 2 mM L-glutamine, 50 U/ml penicillin and 50 μg/ml streptomycin (Sigma-Aldrich).

RT-PCR. Total RNA was extracted from cultured HaCaT cells and primary keratinocytes using the RNeasy Mini kit (Qiagen). RNA (1 μg) was reverse transcribed using AMV Reverse Transcriptase (Promega) and oligo$(dT)_{15}$ (Roche Diagnostics). We used 1 μl of the reaction mix in subsequent PCR with Expand High Fidelity PCR buffer containing 1.5 mM $MgCl_2$ and 0.5 U of High Fidelity DNA Polymerase (Roche Diagnostics). Primers AAGAB5intFor and AAGAB8intRev (see **Supplementary Table 5**) were used to amplify a 292-bp fragment with the following cycling conditions: 1 cycle at 94 °C for 5 min; 35 cycles at 94 °C for 30 s, 52 °C for 30 s and 72 °C for 30 s; and a final extension at 72 °C for 5 min.

Isolation of RNA and gene expression analysis. RNA was isolated from abdominal skin, primary keratinocytes, and HaCaT and HeLa cells using the RNeasy Mini kit and was treated with RNase-Free DNase (Qiagen) to remove any contaminating genomic DNA. We reverse transcribed 1 μg of each using the High-Capacity cDNA Reverse Transcription kit (Applied Biosystems). Then, 1 μl of each reaction was used in quantitative PCR performed with Perfecta qPCR ToughMix, ROX (Quanta Biosciences) on a 7900HT Fast Real-Time PCR system (Applied Biosystems). TaqMan Gene Expression Assays (Life Technologies) for *AAGAB* (Hs01027607_m1) and *GAPDH* (4310884E) were used according to the manufacturer's recommendations.

Multiple-tissue expression analysis. A cDNA clone was generated and used to produce a standard curve for copy-number estimation by qRT-PCR. To make this construct, cDNA was generated by reverse transcription of RNA from HaCaT cells and was used as a template for the amplification of a 940-bp *AAGAB* cDNA fragment using the primers P34clone1 and P34clone2 (**Supplementary Table 5**). The cDNA was cloned as a fragment flanked by EcoRI and HindIII restriction endonuclease sites and was inserted into pcDNA3.1(-)/*myc*-His A (Life Technologies). A normalized cDNA panel from 48 different human tissues (Origene Technologies) was quantified by TaqMan Gene Expression Assay Hs01027607_m1. The standard used in this assay was plasmid DNA encoding wild-type *AAGAB*. The standard curve was calculated using the formulae described by Applied Biosystems.

siRNA knockdown of *AAGAB* in HaCaT cells. siRNA oligonucleotides targeting *AAGAB* and a scrambled negative control were obtained from Eurofins MWG Operon. The sequences of the siRNAs specific for *AAGAB* (designated AAGAB1239 and AAGAB2164) and the non-specific control siRNA (designated NSC4; a scrambled bacterial *lacZ* sequence) are shown in **Supplementary Table 5**. We plated 1.2×10^5 HaCaT cells in each well of a 6-well dish containing DMEM supplemented with 10% FCS and transfected the cells with siRNA at a final concentration of 5 nM using Lipofectamine RNAiMAX Reagent (Invitrogen). Cells were incubated for 72 or 96 h before harvesting for RNA extraction and protein isolation and for cell proliferation analysis.

Cell proliferation analysis. HaCaT cells were transfected with siRNA and incubated for 96 h. Cells were washed with PBS and detached from the dishes using 0.05% trypsin-EDTA. Counts of viable cells (after trypan blue staining) were obtained using a hemocytometer.

Antibodies to α- and γ-adaptin–binding protein p34. Two affinity-purified rabbit polyclonal antibodies, p34-1 and p34-2, were raised using a glutathione S-transferase (GST) fusion protein consisting of residues 142–315 (the C terminus) of rat α- and γ-adaptin–binding protein p34 (85% identical and 91% similar to the human protein). These antibodies were used for the HeLa cell experiments (protein blot analysis and immunofluorescence). For the HaCaT cell experiments, rabbit polyclonal antibody to α- and γ-adaptin–binding protein p34 was used (HPA040174, Sigma-Aldrich). Protein blotting and immunofluorescence of HeLa cells was repeated using the Sigma-Aldrich antibody with very similar results (data not shown). Similarly, protein blotting and immunofluorescence of HaCaT cells was repeated using p34-2 with similar results (data not shown).

Protein blotting of HaCaT lysates and EGFR quantification. Cells were rinsed in ice-cold PBS, lysed in SDS lysis buffer (1% SDS, 20 mM Tris-HCl, pH 8.0, 137 mM NaCl, 10% glycerol, 2 mM EDTA) with added protease inhibitor cocktail (Sigma-Aldrich), phosphatase inhibitor cocktail (Sigma-Aldrich) and 25 U/ml Benzonase (Merck) and incubated at room temperature for 10 min with agitation. Lysates were cleared by centrifugation at 10,000*g* for 10 min at 4 °C, and protein concentration was determined using the Bio-Rad Protein Assay. For each sample, 10 μg of total protein was separated on NuPAGE 4–12% Bis-Tris polyacrylamide gels (Invitrogen) in NuPAGE MOPS running buffer (Invitrogen) and blotted onto Hybond-C Extra (GE Healthcare). Membranes were probed with a 1:1,000 dilution of the appropriate primary antibody (rabbit antibody to α- and γ-adaptin–binding protein p34, Sigma-Aldrich), rabbit antibody to EGFR (4267P, Cell Signaling Technology) or a 1:10,000 dilution of mouse antibody to β-actin (A5441, Sigma-Aldrich). Membranes were then incubated with a 1:1,000 dilution of horseradish peroxidase (HRP)-conjugated goat secondary antibody to rabbit or HRP-conjugated rabbit secondary antibody to mouse (Dako). Immobilon Western Chemiluminescent HRP substrate (Millipore) was used for visualization. For detection of phosphorylated EGFR, blots were blocked in 3% BSA in PBS containing 0.1% Tween-20 (PBST) and 10 mM β-glycerophosphate for

© 2012 Nature America, Inc. All rights reserved.

1 h at room temperature and incubated overnight in a 1:1,000 dilution of antibody to phosphorylated EGFR (Tyr992; 2235, Cell Signaling Technology) in PBST containing 10 mM β-glycerophosphate at 4 °C. Blots were washed in three changes of PBST containing 10 mM β-glycerophosphate and incubated in a 1:1,000 dilution of HRP-conjugated goat secondary antibody to rabbit in PBST containing 10 mM β-glycerophosphate for 1 h at room temperature. After washing, blots were developed using enhanced chemiluminescence (ECL). For detection of β-actin, blots were blocked and antibodies were diluted in 5% non-fat milk in PBST under the same conditions as described above. A dilution of 1:10,000 was used for the antibody to actin (Sigma-Aldrich), and a 1:1,000 dilution was used for the secondary HRP-conjugated rabbit antibody to mouse. Quantification of protein bands on blots was performed using a LI-COR Odyssey infrared imaging system.

HeLa cell transfection. Transfection of HeLa cells with siRNA was achieved with Oligofectamine (Invitrogen) following the manufacturer's instructions, using 25 mM siRNA and incubating for 72 h. Knockdown of *AAGAB* was achieved using an siGENOME SMARTpool (M-0159891), and control knockdown was performed with a non-targeting siRNA (D-001810-10) (both from Thermo-Fisher). Transient transfections with plasmid DNA encoding GFP-tagged protein was achieved using HeLa Monster transfection reagent (Cambridge Bioscience) following the manufacturer's instructions and transfecting 48 h before imaging. For immunofluorescence, cells were grown on glass-bottom coverslips (MatTek), fixed in 3% formaldehyde in PBS at room temperature and permeabilized with 0.1% Triton X-100. Cells were imaged with a Zeiss Axiovert 200 inverted microscope using a Zeiss Plan Achromat 63× oil immersion objective, a Hamamatsu ORCA-ER2 camera and Improvision Openlab software (PerkinElmer).

Protein blot, immunofluorescence and immunoprecipitation in HeLa cells. These experiments were performed with antibodies raised in house, including to α- and γ-adaptin–binding protein p34 (p34-1, p34-2), AP-2α, AP-1γ and clathrin heavy chain[10]. Antibody p34-2 was used to detect α- and γ-adaptin–binding protein p34 unless otherwise specified. Constructs encoding N- and C-terminally tagged α- and γ-adaptin–binding protein p34 were constructed from rat cDNA[10] (human and rat AP-1γ share 99% amino-acid identity) by PCR amplification and cloned in frame into pEGFP-N3 (p34-GFP) or pEGFP-C1 (GFP-p34) (plasmids from Takara Bio Europe/Clontech) using HindIII and KpnI restriction sites. The sequences of both constructs were verified by Sanger sequencing analysis.

Immunoprecipitation and clathrin-coated vesicle isolation in HeLa cell extracts. For immunoprecipitation, cells were lysed in PBS containing 1% IGEPAL (Sigma-Aldrich). Lysates were cleared of debris by centrifugation, and antibody-protein complexes were captured using Protein A Sepharose (Pharmacia). Samples were then analyzed by PAGE and protein blotting. Blots were probed with various antibodies, and signals were visualized with the ECL Plus Western Blotting Detection System (GE Healthcare). Control clathrin-coated vesicle–enriched fractions were prepared as described previously[31], except that the final pelleting step was performed at 86,900*g* for 30 min to improve yield.

Ultrastructural analysis. Skin biopsy specimens were cut into small pieces (of <1 mm^3) and fixed in half-strength Karnovsky fixative for 4 h at room temperature. After washing in 0.1 M sodium phosphate buffer (pH 7.4), samples were immersed in 1.3% aqueous osmium tetroxide (TAAB Laboratories) for 2 h. Samples were then incubated in 2% uranyl acetate (Bio-Rad) and dehydrated in a graded ethanol series. We embedded the samples in epoxy resin via propylene oxide (TAAB Laboratories). Ultra-thin sections were stained with uranyl acetate and lead citrate and examined on a Philips CM10 transmission electron microscope.

29. Cottingham, R.W. Jr., Idury, R.M. & Schaffer, A.A. Faster sequential genetic linkage computations. *Am. J. Hum. Genet.* **53**, 252–263 (1993).
30. Schäffer, A.A., Gupta, S.K., Shriram, K. & Cottingham, R.W. Jr. Avoiding recomputation in linkage analysis. *Hum. Hered.* **44**, 225–237 (1994).
31. Hirst, J., Miller, S.E., Taylor, M.J., von Mollard, G.F. & Robinson, M.S. EpsinR is an adaptor for the SNARE protein Vti1b. *Mol. Biol. Cell* **15**, 5593–5602 (2004).

© 2012 Nature America, Inc. All rights reserved.

doi:10.1038/ng.2444

ORIGINAL ARTICLE

Postoperative DAV-IFN-β therapy does not improve survival rates of stage II and stage III melanoma patients significantly

T. Matsumoto,[1,*] K. Yokota,[1] M. Sawada,[1] A. Sakakibara,[1] S. Shibata,[1] S. Yasue,[1] Y. Tomita,[1] H. Yatsuya,[2,3] M. Akiyama[1]

[1]Department of Dermatology, Nagoya University Graduate School of Medicine, Nagoya, Japan
[2]Department of Public Health and Health Systems, Nagoya University Graduate School of Medicine, Nagoya, Japan
[3]Department of Public Health, Fujita Health University, Toyoake, Japan
*Correspondence: Takaaki Matsumoto. E-mail: tmatsumoto@med.nagoya-u.ac.jp

Abstract

Background DAV-interferon (IFN)-β therapy is a combination chemotherapy of dacarbazine (DTIC), nimustine (ACNU) and vincristine (VCR) with local subcutaneous injection of IFN-β that is widely employed as postoperative adjuvant chemotherapy to treat malignant melanoma in Japan. However, the efficacy of DAV-IFN-β therapy has not been confirmed by randomized controlled trials and the benefit of DAV-IFN-β therapy has not been established yet. This study evaluated the contribution of DAV-IFN-β therapy to improve survival of postoperative patients with cutaneous melanoma.

Methods Patients with stage II or III cutaneous melanoma seen at Nagoya University Hospital from January 1998 to December 2009 were eligible for this study. Disease-free survival rates and melanoma-specific survival rates were evaluated. A propensity score was calculated to control for the effects of variables related to decisions regarding the application of DAV-IFN-β therapy.

Results Eighty-two stage II and 60 stage III melanoma patients were included. In the post-matched stage II patients (17 matched pairs), the mean (±SE) disease-free survival rates were 39.9±13.7% for DAV-IFN-β therapy and 73.1±11.7% for non-use (hazard ratio for recurrence, 2.06; 95% CI, 0.63–6.69; $P = 0.23$), and the melanoma-specific survival rates were 66.2±20.0% for DAV-IFN-β therapy and 86.2±9.1% for non-use (hazard ratio for death, 1.09; 95% CI, 0.17–6.82; $P = 0.93$). In the post-matched stage III patients (nine matched pairs), the disease-free survival rates were 29.6±16.4% for DAV-IFN-β therapy and 33.3±15.7% for non-use (0.69; 95% CI, 0.22–2.17; $P = 0.53$), and the melanoma-specific survival rates were 55.6±16.6% for DAV-IFN-β therapy and 44.4±16.6% for non-use (0.67; 95% CI, 0.18–2.50; $P = 0.55$).

Conclusions DAV-IFN-β therapy brought no significant improvement in either disease-free survival rates or melanoma-specific survival rates of patients with stage II or III cutaneous melanoma. A randomized controlled trial would be required to further evaluate the efficacy of DAV-IFN-β therapy as an adjuvant chemotherapy.

Received: 4 July 2012; Accepted: 16 October 2012

Conflicts of interest

None.

Funding sources

None.

Introduction

DAV-interferon (IFN)-β therapy, a combination chemotherapy of dacarbazine (DTIC), nimustine (ACNU) and vincristine (VCR) in combination with local subcutaneous injection of IFN-β, is widely used to treat malignant melanoma in Japan, especially as postoperative adjuvant chemotherapy. DTIC was first introduced in Japan in 1977, and several combination chemotherapies involving it have been performed since then. DAV combination chemotherapy was reported to improve survival rates of melanoma patients in one multicentre study.[1] Clinical trials of natural IFN-β derived from human fibroblasts, commenced in 1978, revealed an efficacy rate of 50% against cutaneous metastasis of malignant melanoma,[2] and use of IFN-β was supported by another study in 1985.[3] To

© 2012 The Authors

further improve the prognosis, the DAV therapy protocol was developed into DAV therapy plus IFN-β, in which DAV is administered in combination with local injection of INF-β (DAV-IFN-β), as a postoperative adjuvant therapy. In 1988, a trial in Japan revealed that the prognosis for malignant melanoma in patients with DAV-IFN-β therapy was better than that for patients with DAV therapy alone, especially among stage III patients.[3] However, the efficacy of DAV-IFN-β therapy has not been established sufficiently, because the above-mentioned studies were not randomized controlled trials, and there seemed to be significant differences in baseline/pretreatment characteristics between the DAV therapy group and the control group, and between DAV-IFN-β therapy groups and patients with simple DAV therapy. Indeed, a randomized trial of adjuvant therapy with DTIC demonstrated no significant effects.[4–6] In the present study, we examined 142 stage II/III cutaneous melanoma patients at our institute to evaluate the contribution of DAV-IFN-β therapy to the improvement of patient prognosis. Propensity score was used to adjust for confounding factors in baseline characteristics.

Patients and methods

Patients

Patients with primary cutaneous melanomas that were classified as stage II or stage III (UICC/AJCC, 2002) seen at Nagoya University Hospital from January 1998 to December 2009 were eligible for this study (142 patients: 82 in stage II; 60 in stage III). All patients underwent wide excision of the primary melanoma, and no patients had chemotherapy or immunotherapy prior to the operation. Except for 17 cases, sentinel lymph node biopsy or lymphadenectomy was performed subsequently or simultaneously. The methods of sentinel lymph node biopsy and pathological evaluation are described elsewhere.[7–11] Patients who had other chemotherapeutic regimens were excluded.

This study was performed according to the principles expressed in the Declaration of Helsinki and the ethics policies of the institution, and was approved by the Ethics Review Committee of Nagoya University Graduate School of Medicine.

DAV-IFN-β protocol and other treatments

As shown in Fig. 1, the DAV-IFN-β therapy recipients were administered DTIC (80–140 mg/m^2, 60-min infusion once a day for five consecutive days), ACNU (50–100 mg/m^2, 30-min infusion on day 1) and VCR (0.5–0.8 mg/m^2, 30-min infusion on day 1) with IFN-β (3×10^6 IU/body, local injection once a day for 10 consecutive days) (Feron®; Toray Industries, Inc., Chuo-ku, Tokyo, Japan). DAV-IFN-β therapy was done every 4 weeks in three cycles for stage II and in five cycles for stage III, in principle. Postoperative maintenance therapy was given to some patients, consisting of local injection of IFN-β. Different from DAV-IFN-β therapy, the main method of this maintenance therapy involves only subcutaneous IFN-β injection around the surgical scar of the primary lesion at a dose of 3×10^6 IU/day every 3–4 weeks for 2–3 years. All patients were monitored postoperatively by means of clinical examinations, blood test and CT or PET/CT at least every 6 months.

Baseline clinical data

Data including those of age, sex, date of first medical examination, site of the primary melanoma, tumour thickness, status of ulceration (with vs. without), treatment history of sentinel lymph node biopsy or lymphadenectomy, status of severe complications (with vs. without) and postoperative performance status (PS) were collected from medical records of the patients at our institute. Regarding tumour thickness and status of ulceration, we excluded cases in which regression was strongly suspected from the present analysis, because tumour thickness did not reflect the disease progression precisely in cases showing regression. Thus, four cases in stage III were excluded from the below-mentioned stratified and matched analysis. Postoperative PS was assessed by the Eastern Cooperative Oncology Group PS scores of 0, 1, 2 and over 2.

For all analyses, patients were divided into two groups: one of DAV-IFN-β therapy use as postoperative adjuvant chemotherapy and the other of non-use.

The primary endpoint among the cohorts was melanoma-specific survival (survival until death from melanoma). The other endpoint was disease-free survival before first recurrence at any site (survival without evidence of recurrence or metastasis). Follow-up and survival periods were calculated from the date of the first medical examination to the date of the last examination or death, until December 2011. Of all the patients, nine patients (four with DAV-IFN-β therapy use and four with non-use in stage II and one with non-use in stage III) were lost between the start of follow-up and December 2011. Survival data or cause and date of death were collected by serial contact with patients and from their medical records.

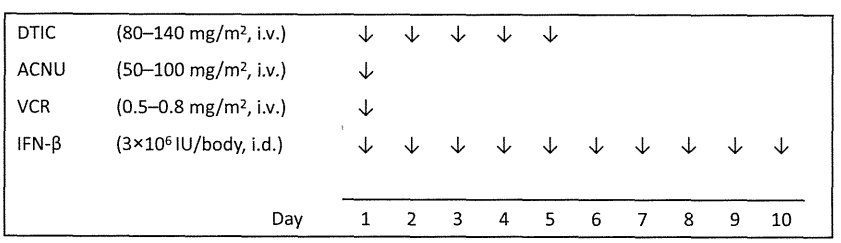

Figure 1 Drug dosage and administration schedule per course of DAV-IFN-β therapy.

© 2012 The Authors
Journal of the European Academy of Dermatology and Venereology © 2012 European Academy of Dermatology and Venereology

Table 1 Baseline characteristics of the patients

	Stage II			Stage III		
	DAV-IFN-β (*N* = 44)	Non-use (*N* = 38)	*P*-value	DAV-IFN-β (*N* = 44)	Non-use (*N* = 16)	*P*-value
Age (years)	60.4 (12.4)	67.3 (16.3)	0.032	58.0 (13.3)	69.3 (10.9)	0.004
Male, *n* (%)	21 (47.7)	18 (47.4)	0.97	24 (54.5)	7 (43.8)	0.46
First medical examination, *n* (%)						
1998–2000	11 (25.0)	3 (7.9)	0.054	8 (18.2)	2 (12.5)	0.90
2001–2003	15 (34.1)	9 (23.7)		9 (20.5)	4 (25.0)	
2004–2006	7 (15.9)	13 (34.2)		16 (36.4)	5 (31.3)	
2007–2009	11 (25.0)	13 (34.2)		11 (25.0)	5 (31.3)	
Primary site, *n* (%)						
Head and neck	6 (13.6)	4 (10.5)	0.182	6 (13.6)	3 (18.8)	0.70
Trunk	4 (9.1)	6 (15.8)		13 (29.5)	5 (31.3)	
Upper extremity	14 (31.8)	5 (13.2)		8 (18.2)	1 (6.3)	
Lower extremity	20 (45.5)	23 (60.5)		17 (38.6)	7 (43.8)	
Tumour thickness (TT; mm)	4.8 (3.1)	5.2 (6.4)	0.81	5.8 (3.8)	7.8 (4.4)	0.13
In situ	0 (0)	0 (0)		0 (0)	0(0)	
TT ≤ 1	0 (0)	0 (0)		1 (2.4)	1 (6.7)	
1 < TT ≤ 2	3 (6.8)	4 (10.5)		5 (12.2)	0 (0)	
2 < TT ≤ 4	24 (54.4)	19 (50.0)		14 (34.1)	2 (13.3)	
4 < TT*	17 (38.6)	15 (39.5)		21 (51.2)	12 (80.0)	
Regression, *n*	0	0		3	1	
Ulceration, *n* (%)	36 (81.8)	26 (68.4)	0.16	26 (63.4)	12 (80.0)	0.24
Regression, *n*	0	0		3	1	
SLNB or lymphadenectomy	39 (88.6)	29 (76.3)	0.14	44 (100)	12 (80.0)	0.002
Severe complication†, *n* (%)	4 (9.1)	17 (44.7)	<0.001	6 (13.6)	7 (46.7)	0.008
Postoperative PS ≥ 2, *n* (%)	4 (9.1)	15 (39.5)	0.001	5 (11.4)	3 (20.0)	0.40
Frequency of DAV-IFN-β	3.25 (1.26)	–	–	3.84 (1.48)	–	–
IFN-β maintenance therapy, *n* (%)	23 (52.3)	26 (68.4)	0.14	25 (56.8)	14 (87.5)	0.028

†Severe complications were defined by following criteria: hepatic complication, serum albumin ≤3.5 g/dl, total bilirubin ≥2.0 mg/dl and/or prolonged prothrombin time (PT); renal complication, glomerular filtration rate (GFR) ≤60% and/or similarity of chronic kidney disease (CKD); respiratory complication, active asthma and/or chronic obstructive pulmonary disease (COPD); cardiovascular complication, New York Heart Association (NYHA) classification class ≥II; and neuropsychiatric complication, dementia that needs fulltime support.
SLNB, sentinel lymph node biopsy; PS, performance status.

Statistical analysis

Continuous variables were expressed as mean (standard deviation) and were compared using the Student's *t*-test. Categorical data were displayed as frequencies and percentages, and were compared using the Chi-squared test. Because patients were not randomly assigned to DAV-IFN-β therapy use or non-use, there were significant differences in baseline covariates between the two groups. Therefore, we used propensity score analyses to control for potential confounding effects of differences in the pretreatment characteristics of DAV-IFN-β therapy use vs. non-use. A propensity score is a measure of the likelihood that a patient will be assigned to DAV-IFN-β therapy or not on the basis of the patient's pretreatment characteristics. To calculate a propensity score for each patient, we estimated the probability that each patient would receive DAV-IFN-β therapy by using logistic regression analysis. Variables included in the logistic model were all the baseline clinical data described above. However, distribution in the variable of sentinel lymph node biopsy or lymphadenectomy was so deflected that we excluded these variables from the model for calculating propensity score. The number of treatment cycles and the presence or absence of postoperative IFN-β maintenance therapy were not included in the multivariate logistic regression analysis because they were post-chemotherapeutic factors and had no effect on decisions regarding DAV-IFN-β therapy. Propensity scores were categorized into four groups by quartiles.

We assessed the relationship between DAV-IFN-β therapy use and study outcome variables by three methods: (i) crude comparison without regard to propensity score; (ii) stratified analysis (crude comparison for each propensity score quartile); and (iii) matched analysis (comparison of survival between propensity score quartile-matched patients with DAV-IFN-β therapy use vs. non-use). For the matched analysis, the number of pairs was

© 2012 The Authors

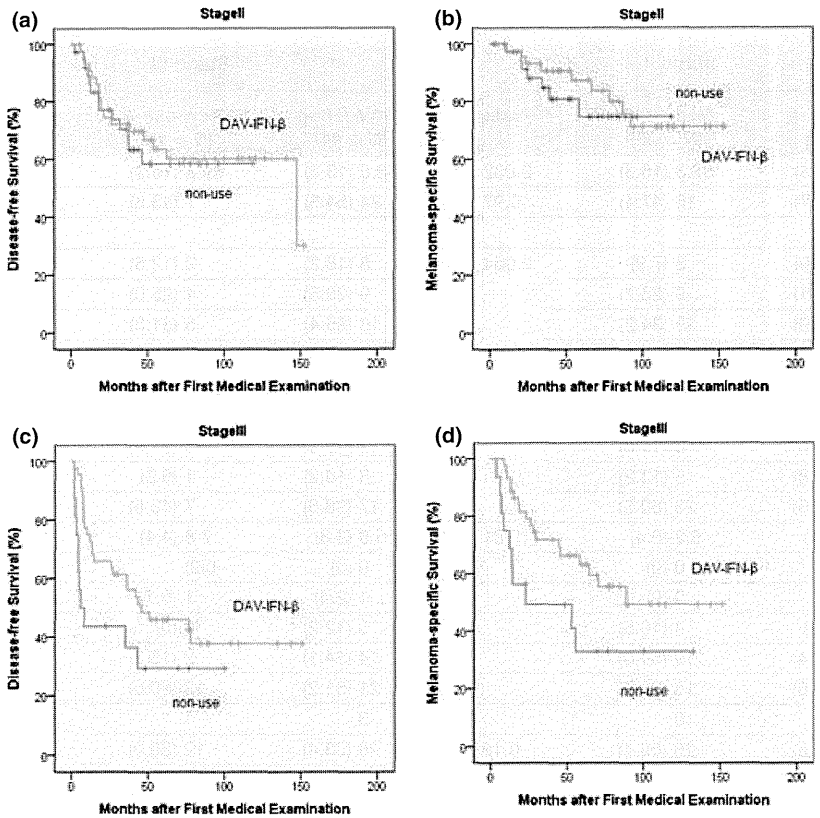

Figure 2 Disease-free survival and melanoma-specific survival in the crude comparison. Disease-free survival (a) and melanoma-specific survival (b) in stage II. Disease-free survival (c) and melanoma-specific survival (d) in stage III. The melanoma-specific survival rate in stage III is higher with DAV-IFN-β therapy use than with non-use, although no significant difference is observed in the disease-free survival rate or the melanoma-specific survival rate either in stage II or stage III. Green dots and lines, patients with DAV-IFN-β therapy; blue dots and lines, patients without DAV-IFN-β therapy.

Table 2 Hazards ratio of DAV-IFN-β therapy

	Pre-match				Post-match	
	Crude		Stratified			
	HR(95% CI)	*P*-value	HR (95% CI)	*P*-value	HR (95% CI)	*P*-value
Stage II						
Disease-free	0.87	0.71	1.74	0.37	2.06	0.23
	0.42–1.81		0.52–5.77		0.63–6.69	
Melanoma-specific	0.72	0.53	1.35	0.73	1.09	0.93
	0.26–1.99		0.25–7.27		0.17–6.82	
Stage III						
Disease-free	0.52	0.070	0.55	0.26	0.69	0.53
	0.25–1.06		0.19–1.55		0.22–2.17	
Melanoma-specific	0.47	0.053	0.45	0.21	0.67	0.55
	0.21–1.01		0.13–1.56		0.18–2.50	

HR, hazards ratio; CI, confidence interval.

determined as the number of patients in the smaller of the paired groups (DAV-IFN-β use vs. non-use) for each propensity quartile. Patients in the larger of the two groups (DAV-IFN-β use vs. non-use) were selected randomly for each propensity score quartile.

Kaplan–Meier survival analysis with a log-rank test was used to estimate the mean (±standard error of the mean) disease-free survival rates (no recurrence) and melanoma-specific survival rates (no death from melanoma). For the latter analysis, cases who died from causes other than melanoma were censored at the time of death. In addition, Cox proportional hazard models were also used to estimate the potential benefit of DAV-IFN-β therapy against study outcome variables.

A *P*-value of <0.05 was considered significant. All data were analyzed using SPSS for Windows (SPSS Statistics Version 19; IBM, Armonk, NY, USA).

© 2012 The Authors